공학박사학위논문

Synthesis and Characterization of Biocompatible Polymers for 2D Electronic Device and 3D Scaffold Applications

생체적합성 고분자의 합성과 분석 및 2차원 전자기기와 3차원 스캐폴드로의 적용

2019년 2월

서울대학교 대학원

화학생물공학부

김 나 경

Synthesis and Characterization of biocompatible polymers for 2D electronic device and 3D scaffold applications

by

Na Kyung Kim

Adviser: Professor Jong-Chan Lee, Ph. D.

Submitted in Partial Fulfillment
of the Requirements for the Degree of
DOCTOR OF PHILOSOPHY

February, 2019

School of Chemical and Biological Engineering
College of Engineering
Graduate School
Seoul National University

Abstract

Synthesis and Characterization of biocompatible polymers for 2D electronic device and 3D scaffold applications

김 나 경 (Na Kyung Kim)

공과대학 화학생물공학과 (Chemical and Biological Engineering)

고분자 합성 전공 (Polymer Synthesis)

The Graduate School

Seoul National University

This study presents the synthesis and characterization of biocompatible polymers for 2D electronic device and 3D scaffolds. Firstly, Polymer blends with both biocompatibility and organic thin film transistor (OTFT) characteristics are developed by mixing a biocompatible polymer, poly(2-(2-acetoxyacetyl)ethyl methacrylate) (PHEMAAA) and a conducting polymer, poly(3-hexyl thiophene) (P3HT) at different weight ratios (i.e. P3HT/PHEMAAA = 75/25, 50/50, 25/75). Their OTFT performances were maintained at a similar level to those of pristine P3HT in spite of adding an insulator in the form of PHEMAAA. On the other hand, the biocompatibility of the P3HT/PHEMAAA blend films was found to be

as good as that of PHEMAAA, indicating the successful contribution of the biocompatible polymer. In particular, these combined properties were optimized at a 25/75 weight ratio as described above. These results could be correlated with surface properties such as molecular orientation, morphology, and composition that change upon blending. Such P3HT/PHEMAAA blends are promising materials for applications in biomedical fields where materials come into contact with the human body.

Secondly, A cardanol-based polymer, poly(2-hydroxy-3-cardanylpropyl methacrylate) (PHCPM), was utilized as the gate dielectric of an OTFT. PHCPM has good surface properties, appropriate gate dielectric characteristics, and good compatibility with solution-processed semiconducting polymers. The electrical properties of an FET that was prepared with natural resource-based PHCPM as a gate dielectric layer and solution-processed poly[2,5-bis(3-dodecylthiophen-2-yl)thieno[3,2-b]thiophene] (PBTTT) as a semiconducting layer were investigated on flexible substrates. The flexible PBTTT-OTFT device with the PCHPM gate dielectric exhibited high mobility and reliable performance, even in the bending state, without significant hysteresis.

Finally, a mechanically tissue-like, biocompatible vitrimer film for tissue engineering scaffold applications is presented. 3D hierarchical scaffolds are prepared from the 2D vitrimer film via transesterification-induced hot embossing

patterning and additional reconfiguration process. Microsized grooves patterned on the vitrimer surface are found to enhance C2C12 cell elongation and alignment for promoted muscle regeneration.

Keywords: Biocompatible polymer, blending, tissue-engineering, crosslinking structure, vitrimer, OTFT, 3D scaffold, micropattern

Student Number: 2015-30209

TABLE OF CONTENT

Polymer-based OTFTs upon

Blending with Biocompatible Polymer

Chapter 3

Natural Resource-Based Polymeric Dielectric

for Flexible OTFT System

Chapter 4

Biocompatible Vitrimer Film

for 3D Hierarchical Scaffold Application

List of Tables

List of Figures

Figure 2.7. FE-SEM images of P3HT/PHEMAAA blend films a)-c) before and d)-f) after selective dissolution of PHEMAAA part using THF. (scale bar = 1 um) The connective networks of P3HT domain were observed from all blend surfaces by measuring the film morphologies obtained after selective dissolution of PHEMAAA.

Figure 2.8. The representative XPS S_{2p} and O_{1s} core level spectra on the surfaces of a) 25/75 blend and b) O/S ratios of P3HT/PHEMAAA blend films before (black square line) and after MCB treatment (red triangle line).

Figure 2.9. Representative optical microscopy images of HDFs cultured for 4 days on a) P3HT, b) 75/25 blend, c) 50/50 blend, d) 25/75 blend, e) PHEMAAA films, and (f) the quantitative results (scale bar = 100 um).

Figure 2.10. CLSM images presenting FDA/EB staining on HDFs cultured for 4 d on a) P3HT, b) 75/25 blend, c) 50/50 blend, d) 25/75 blend, and e) PHEMAAA films (scale bar = 100 um).

Figure 3.1. OFET device geometry with the chemical structures of PHCPM and PBTTT.

Figure 3.2. a) Schematic illustration of thermally crosslinked PHPCM and b) FTIR spectra of C-H stretching region of PHCPM films.

Figure 3.3. **AFM height image (10 um × 10um) of the PHCPM film**.

Figure 3.4. a) Capacitance-frequency and b) leakage current density-voltage characteristics of the PHCPM film. The dielectric constant dependency on the frequency is shown in the inset of a).

Figure 3.5. GIWAXD 2D pattern of the PHCPM film.

Figure 3.6. a) Output curves and b) Transfer curves obtained from PBTTT-OFET devices with the PHCPM gate dielectric.

Figure 3.7. a) A photograph of the flexible PBTTT-OFET device with the PHCPM gate dielectric. b) Output curves and c) Transfer curves ofthe flexi ble PBTTT-OFET device obtained in the bending state with a radius of 15 mm.

Figure 4.1. Schematic illustration of PAB-GPOSS vitrimer based on Zn^{2+}-catalyzed transesterification.

Figure 4.2. FT-IR spectra of the PAB-POSS vitrimer, PAB, and POSS in the wavenumber ranges of a) 950-800 cm^{-1} and b) 1800-1600 cm^{-1}, respectively.

Figure 4.3. a) TGA thermogram of the PAB-POSS vitrimer and b) DSC traces of PAB and PAB-POSS vitrimer

Figure 4.4. a) A representative stress-strain curve and b) cyclic stress-strain curves (strain limit = 50 %) of the PAB-POSS vitrimer.

Figure 4.5. DMA curves of the PAB-POSS vitrimer.

Figure 4.6 a) Normalized stress relaxation of the PAB-POSS vitrimer at different temperatures. The dashed line indicates $G/G_0 = e^{-1}$ (≈37 % of the initial stress). b) Arrhenius plot of the measured relaxation times for the PAB-POSS vitrimer.

Figure 4.7. a) Schematic illustration for the fabrication of 3D hierarchical TE scaffolds from the PAB-POSS vitrimer via hot embossing techanique and thermal reconfiguration. Representative SEM images of the b) PAB-POSS vitrimer and micro-patterned PAB-POSS vitrimers with c) 80, d) 40, and e) 10 um groove width, respectively (scare bar= 20 um). f) Various 3D structures constructed by the PAB-POSS vitrimer (scare bar = 0.5 cm). g) A photograph of the tubular structure constructed by the 10 um patterned vitrimer film, which shows an unclear color at a certain light angle.

Figure 4.8. Representative SEM images of the cross-sections of PAB-POSS vitrimers with a) 80, b) 40, and c) 10 um groove widths, respectively. The cross-sections were obtained by FIB milling technique and the depth of each sample was measured at a tilted stage.

Figure 4.9. a) Cell viability of C2C12 cells cultured for 24 and 48 h on the glass substrate and the PAB-POSS vitrimer. Representative SEM images showing the morphology of C2C12 cells cultured for 24 h on the b) PAB-POSS vitrimers, and micro-patterned PAB-POSS vitrimer with c) 80, d) 40, and e) 10 groove width, respectively (scale bar = 20 um). f) Aspect ratios of the C2C12 cells cultured for 24 h on the PAB-POSS vitrimer and micro-patterned PAB-POSS vitrimers.

Figure 4.10. Quantitative analysis of the cell alignment on the a) pristine PAB-POSS vitrimer, and micro-patterned PAB-POSS vitrimers with b) 80, c) 40, and d) 10 um groove widths, respectively.

Introduction

1.1 Biocompatible polymers for various applications

Biocompatibility is the ability to interact with host tissues with a minimal toxic response. Various polymers having biocompatible moieties have been specifically designed for a variety of applications ranging from everyday life to biomedical fields [1].

Biocompatible polymers such as polypropylene (PP), polyethylene (PE), and polystyrene (PS) are commonly used in food and cosmetic containers, taking advantages of their thermal processability [2,3]. In addition to excellent biocompatibility and antifouling property, polybutadiene, fluorinated polymer, and silicon-based rubbers also are responsible for sufficient mechanical property to medical gloves or grafts [4,5].

Polyethylene glycol (PEG), polycaprolactone (PCL), and polylacticacid (PLA) have been widely used in various tissue-contacting applications. Particularly, PCL and PLA are polyether compound that can be biodegraded by hydrolysis, thereby having received much attention from implanted scaffolds and drug delivery system [6].

Recently, natural resources have been emerged as promising biocompatible materials [7]. Cardanol is a natural resource that can be obtained from cashew nut oil [8]. In the previous study, a biocompatible polymer containing cardanol moiety was successfully synthesized and utilized as an antibacterial coating film [9].

1.2. Design of biocompatible polymers from 2D to 3D structures

Biocompatible polymers have been often coated onto various medical devices to improve blood biocompatibility without causing inflammation [1]. Extending the current limit of application as coating material, there is an increasing demand to develop 2-dimensional (2D) flexible films and further 3D structures using biocompatible polymers for practical use in biomedical applications in contact with human tissues.

Flexible 2D films have been successfully employed to dermal patches for wound-healing [10]. In addition, 2D electronic devices such as organic thin-film transistors (OTFTs) have been implanted into human skin or tissues as biosensors for diagnostics and health-monitoring, since they show amplified electronic signals in response to minimal stimulation by the analytes [11].

3D structures of the biocompatible polymers make them ideally suited for implantable scaffolds that can mimic the 3D microenvironment as in native tissues and organs [12]. Those biomimetic 3D scaffolds have been prepared by several methods such as incorporation of the fiber and porous structures into biocompatible polymers using electro-spinning or 3D printing [13].

Therefore, suitable polymeric materials to satisfy the supportive mechanical

strength as well as sufficient biocompatibility are highly required for various biomedical applications.

1.3. Motivation

Herein, we present the synthesis of biocompatible polymers for 2D electronic device and 3D scaffold applications. Firstly, biocompatible OTFT system was developed by introducing a biocompatible polymer and a natural resource-based polymer into semiconducting and dielectric layer, respectively, for implantable applications. A biocompatible polymer, poly(2-(2-acetoxyacetyl)ethyl methacrylate) (PHEMAAA) was synthesized by introducing ester-linkage containing side chains to Poly(2-hydroxyethyl methacrylate) (PHEMA) through simple esterification [14]. Blend films with both biocompatibility and semiconducting property were prepared by mixing PHEMAAA and poly(3-hexyl thiophene) (P3HT) for OTFT application. In addition, a cardanol-based polymer, poly(2-hydroxy-3-cardanylpropyl methacrylate) (PHCPM) [9] was utilized as the gate dielectric to enhance the biocompatibility of a flexible OTFT system. It is expected that such biocompatible OTFT system might be integrated into human body as a biosensor, which enables a wide range of biomedical applications from prosthetics to health-monitoring [11].

Furthermore, a rubber-based vitrimer film having sufficient biocompatibility and

mechanical properties was prepared for 3D hierarchical scaffold application. The reconfigurability of the vitimer film based on thermally induced transesterification facilitates post micropatterning and further construction into 3D structures. In particular, the 3D hierarchical structures can precisely control the biological cell activities including cell morphology, growth, migration, and consequently differentiation [15]. Therefore, the vitrimer film might have a huge potential to be widely used as the 3D scaffold for tissue repair.

1.4. References

[1] V. P. Shastri, Current Pharmaceutical Biotechnology, 2003, 4, 331-337.

[2] E.B. Mathiesen, U. Lindgren, F. P. Reinholt, and E. Sudmann, Acat Orthop. Scand., 1986, 57, 193-196.

[3] S. Anwar, Hospt. Med., 2003, 64, 34-35.

[4] W. Becker, and B.E. Becker, Periodontol. 2000, 1, 46-53.

[5] De Coster N, and Magg H. Kautschuk Gummi Kunststoffe, 2003, 7, 405–411.

[6] J. Zhao, D. Pahovnik, Y. Gnanou, and N. Hadjichristidis, Polym. Chem., 2014, 5, 3750-3753.

[7] M. Irimia , V.A. Troshin, M.Reisinger, L. Shmygleva, Y. Kanbur, G. Schwabegger, M.Bodea, R. Schwödiauer, Adv. Funct. Mater. 2010, 20, 4069–4076.

[8] D.G. Kim, H. Kang, Y.S. Choi, S. Han, J.C. Lee, Polym. Chem., 2013, 4, 5065-5073.

[9] Y.S. Choi, K.H. Kim, D.G. Kim, H.J. Kim, S.H. Cha, J.C. Lee, RSC Adv., 2014, 4, 41195-41203.

[10] K.Kataria, A.Gupta, G.Rath, R.B.Mathur, S.R.Dhakate, Int. J. Pharm., 2014, 469, 102-110.

[11] A. N. Sokolov, B. C-K. Tee, C. J. Bettinger, J. B.-H. Tok, and Z. Bao, Acc. Chem. Res. 2012, 45, 361–371.

[12] R.G. Flemming, C.J. Murphy, G.A. Abrams, S.L. Goodman, and P.F. Nealey, Biomaterials, 1999, 20, 573-588.

[13] S. Fleischera, A.Shapiraa, R. Feinera, and T. Dvir, PNAS, 2017, 114, 1898–1903.

[14] E-H. Sohn, J. Ahn, S. H. Bhang, J. Kang, J. Yoon, B-S. Kim, J-C. Lee, Macromol. Biosci. 2012, 12, 211–217.

[15] L. Downing, J. Soto, C. Morez, T. Houssin, A. Fritz, F. Yuan, J. Chu, S. Patel, D.V. Schaffer, and S. Li, Nat. Mater., 2013, 12, 1154–1162.

Chapter 2

Enhanced Biocompatibility in the Semiconducting Polymer-based OTFTs upon Blending with Biocompatible Polymer

2.1. Introduction

Organic thin-film transistors (OTFTs) have been investigated by many research groups because of their numerous potential applications, ranging from flexible backings in active matrix displays to item-level radiofrequency identification tags [1–3]. Recently, continued research on OTFTs has demonstrated their potential as a sensor platform, utilizing their effective transduction mechanism that can transform even a small induced external stimulus into more amplified electric signals [4]. With high sensitivity, OTFT based-sensors are considered to be a strong candidate for disposable miniaturized chips, important for biomedical diagnostics, and can be used in both drug screening and toxicity tests [5,6]. This biomedical test system is highly dependent on the biocompatibility and non-toxicity of the active layer for cell cultivation and long-term reporting without an inflammatory response [7,8]. Therefore, several attempts to improve the biocompatibility of conducting polymers have been performed by blending the polymers with biomolecules, doping them with bioactive molecules, hydrogelation, and oxygen plasma treatment [9–12].

Among these techniques, blending is one of the most effective methods and can easily combine the beneficial properties of each component into one blended material. This method generally dominates over other chemical

modifications of conducting polymers, in that it does not require any tedious or time-consuming processes. Several drawbacks of conducting polymers, such as low biocompatibility, mechanical strength, air stability, and high costs, could be mitigated by adding insulating polymers with high performance [13–15]. However, conducting polymers blended with insulating polymers often suffer from degradation in device performances due to dilution effects [16]. The dilution effect, however, can be overcome by connecting the conductive polymeric domains in the insulating polymer matrix through vertical phase-separated structures or nanowire networks [17,18]. By controlling the blend structure, blending methods could be even more widely applicable and further reduce semiconductor costs. P3HT is one of the more commonly used conducting polymers for OTFT systems, because it has high mobility (10-4 to 10-2 cm2 V-1 s-1) and good solubility in common solvents [19]. However, the use of P3HT in biomedical applications can be limited due to their poor cell adhesion properties [9]. There have been only a few studies of the improvement of biocompatibility of P3HT by blending with biocompatible insulating polymers, but these blends still suffer a loss in the conducting properties of P3HT.20 In this work, we impart biocompatibility into a P3HTbased OTFT system by blending it with poly(2-(2-acetoxyacetyl) ethyl methacrylate) (PHEMAAA),

without any loss of the OTFT properties of P3HT. Previously, PHEMAAA was successfully synthesized and its excellent biocompatibility has been demonstrated [21]. We believe that this is the first report demonstrating a biocompatible polythiophene system with acceptable
OTFT performance created using a blending method.

2.2. Experimental

2.2.1. Materials

Poly(2-hydroxyethyl methacrylate) (PHEMA) (Mw = 300,000 $gmol^{-1}$) was purchased from Scientific Polymer Products (Ontario, NY, USA). Regioregular P3HT was obtained from Sigma-Aldrich (Mw = 50 000). Hexamethyldisilazane (HMDS) (99%) and acetoxyacetyl chloride (97%) were purchased from Sigma-Aldrich. Chloroform ($CHCl_3$, 99.5%) and monochlorobenzene (MCB, 99.5%) purchased from Sigma-Aldrich were used as received. Microscope cover slides (25 mm) were purchased from Marienfeld GmbH & Co. KG (Lauda-K¨onigshofen, Germany). PHEMAAA, as shown in Figure 2.1, was synthesized according to previously reported procedures [21]. Briefly, PHEMA (500 mg) was dissolved in 3mL of pyridine, then acetoxy acetyl chloride (1.2 equiv.) diluted with 3 mL of tetrahydrofuran (THF) was added dropwise to the solution. The reaction proceeded for 12 h at room temperature, and the product could be obtained after several precipitation using water and methanol.

2.2.2. Preparation of polymer blend films

1 wt% of P3HT, PHEMAAA, and their mixtures of P3HT and PHE MAAA with different mole ratios of 75/25, 50/50, and 25/75 were di ssolved in a 1:1 (v/v) solvent mixture of $CHCl_3$ and MCB. Both P3H T and PHEMAAA are well-dissolved in $CHCl_3$, however, the mixture of $CHCl_3$ and MCB was used as a solvent, because the poor solubilit y of P3HT in MCB could result in well-aligned P3HT crystal orientat ion, which can lead to favourable OTFT performance [22]. The poly mer solutions were sonicated at 40 ^{o}C until the solutions become tran sparent. Silicon wafers were cleaned in a piranha solution (a mixture of concentrated sulfuric acid and hydrogen peroxide in a 7:3 ratio by volume) for 2 h followed by rinsing with ethanol (EtOH) and drying under nitrogen flow. The cleaned silicon wafers were treated with H MDS at 100 ^{o}C for 1 h to make their surfaces hydrophobic. The pol ymer solutions, filtered through a 0.45 um PTFE syringe filter, were t hen spin-coated onto the HMDS modified silicon wafers for morpholo gy analysis, using a Laurell model WS-400A-6NPP/LITE spin coater a t a rate of 3000 rpm for 30 s. The polymer films, having P3HT and PHEMAAA in the ratios of 75/25, 50/50, and 25/75, are named as75/ 25 blend, 50/50 blend, and 25/75 blend, respectively. For cell tests,all

samples were prepared as described above but on the glass substrates.

2.2.3. Surface characterization

Grazing incidence wide-angle X-ray diffraction (GIWAXD) was perfor med using a high-power X-ray beam (photon flux ≈ 10^{11} photons s^{-1} $mrad^{-1}$ per 0.1%, beam size ≤ 0.5 mm2) from a synchrotron radiation source (3C beamline, Pohang Accelerator Laboratory, Korea) at λ= 1. 1352 Å). The detection system was equipped with a 2D X-ray detect or (PI-SCX4300-165/2, Princeton Instruments). The scattering angles w ere corrected according to the positions of the X-ray beams reflected from the silicon substrate interface with changing incidence angle (α_i), and with respect to pre-calibrated silver behenate ($AgC_{22}H_{43}O_2$). The s urface topologies of the polymer films were obtained using tapping-m ode atomic force microscopy (AFM; SPA 400 with a SPI 3800 contr oller, Seiko Instruments Industry, Co. Ltd., Japan) using a siliconnitrid e cantilever (NCH Point Probe, Nano world, Neuchtel, Switzerland) w ith a resonance frequency of 320 kHz and a spring constant of 42 N m^{-1}. The root-mean-square (RMS) roughness values were taken from t he topography images of a 5 × 5 um^2 area at room temperature. X-r

ay photoelectron spectroscopy (XPS) experiments were performed in a n UHV multipurpose surface analysis system (Thermo Scientific, Sigm a Probe, UK) operating at base pressures $<10^{-10}$ mbar. For acquisition of photoelectron spectra, the constant analyzer energy (CAE) mode w as employed at a pass energy of 40 eV and a step of 0.1 eV at a ta keoff angle of 90^{o}.

Since the annealed P3HT is not soluble in tetrahydrofuran (THF) but PHEMAAA is well-dissolved in THF, the selective dissolution of the PHEMAAA in the 25/75 blend film was successfully performed. The 25/75 blend film morphologies before and after dissolution of PHEMAAA were characterized using a FE-SEM. (JEOL JSM-6701F)

The contact angles of deionized water and diiodomethane (MI) were measured at room temperature and ambient relative humidity using a Kruss DSA 10 contact angle analyzer interfaced to drop shape analysis software. The Owens-Wendt-Rabel-Kaelble (OWRK) method [23] was used to calculate the surface energy of the polymer films.

2.2.4. OTFT characteristics

Bottom-gate, top-contact devices were fabricated on highly doped p-ty

pe Si with a 300 nm SiO_2 dielectric layer. Silicon wafers were clean ed by sonication of the substrates in acetone and isopropyl alcohol (I PA), followed by drying with nitrogen. The silicon wafers were then treated with atmospheric oxygen plasma for 5 min at a fixed RF pow er of 100 W at a frequency of 13.56 MHz (Emitech K1050X). Argon (5 Lpm) and oxygen (20 sccm) were used as the carrier and reactive gases, respectively. After plasma treatment, Si/SiO_2 was hydrophobicall y treated with hexamethyldisilazane (HMDS) to prevent charge trappin g by R–OH functional groups. The P3HT and P3HT/PHEMAAA blen d solutions with different weight ratios of 75/25, 50/50, and 25/75 we re dissolved at a concentration of 1 wt% in MCB/$CHCl_3$ (1:1 v/v). Fi ltered through a 0.45 um PTFE syringe filter, the solutions were then spun-cast onto the HMDS-modified silicon wafers at a rate of 3000 r pm for 30 s, using a Laurell model WS-400A-6NPP/LITE spin coater, then annealed at 200 ^{o}C for 30 min. All procedures and measurement s were carried out in a glove box under dry argon gas. In order to make electrical contact, source drain electrodes were patterned by plac ing thin steel shadow masks on top of the substrate, and thermally ev aporating a 50 nm gold layer on top. The pressure in the chamber w as maintained at about 10^{-6} mbar and the voltage applied across the h

eating coil controlled to keep evaporation rates of 0.1 $Å s^{-1}$. The devic es were fabricated with variable channel lengths (L) of 20–100 um an d widths (W) of 0.5–2 mm, respectively. The electrical characteristics of the OTFT devices were measured at room temperature under ambi ent conditions using an Agilent 4155C semiconductor parameter analy zer. Typically, several output curves were recorded for different gate voltages, and transfer curves were measured in both the linear and sat uration regimes of the OTFT. Numerical differentiation of IDS with r espect to VGS allows the field-effect transistor mobility (m) to be cal culated in the saturation regimes using eqn (2.1), whereW, L, C_i,and V_t are the channel width, channel length, the capacitance per unitarea of the dielectric layer, and the threshold voltage, respectively. The fiel d-effect mobility values in the saturation region were calculated from the slope of the square root of the drain-source current as a function of the gate-source voltage, i.e. $|I_{Dsat}|^{1/2}$ versus V_g plot (eqn (1)). Avera ge data were calculated from analysis of 10 independent devices.

$$I_{Dsat} = \frac{WC_i}{2L}\mu(V_{GS} - V_T)^2 \qquad (2.1)$$

2.2.5. Cytotoxicity tests

Human dermal fibroblasts (HDFs) were cultured in Dulbecco's modified Eagle's medium (DMEM, Gibco BRL, Gaithersburg, MD, USA) supplemented with 10% (v/v) fetal bovine serum (FBS, Gibco BRL) and 100 units per mL penicillin (Gibco BRL) and 100 mg mL^{-1} streptomycin (Gibco BRL). To test the biocompatibility of P3HT, PHEMAAA, and their blend films, cells were seeded on polymer films at a density of 5×10^3 cells per cm^2 and maintained in DMEM (Gibco BRL) supplemented with 10% (v/v) FBS (Gibco BRL), 100 units per mL penicillin (Gibco BRL), and 100 mg mL^{-1} streptomycin (Gibco BRL). The viability of the HDFs was evaluated using a colorimetric test based on the uptake of neutral red (3-amino-7-dimethylamino-2-methylphenazine hydrochloride) dye into viable cells. In brief, HDFs were rinsed with phosphate-buffered saline (PBS, Sigma Aldrich, St. Louis, MO, USA) and incubated for 3 h at 37 ^oC in DMEM containing neutral red (50 mg mL^{-1}, Sigma). After removing the medium, a solution of 1% (v/v) acetic acid and 50% (v/v) ethanol was added to extract the dye. After 5 min of incubation at room temperature, the absorbance was read at 540 nm. The viability of the HDFs was expressed as a percentage of the absorbance of a PHEMAAA-positive control. On day4, the morphology of HDFs was evaluated using light microscopy (IX71,

Olympus, Tokyo, Japan). Live and dead cells were detected with fluo rescence microscopy (DS-2U, Nikon, Japan) after staining with fluores cein diacetate (FDA, Sigma Aldrich) and ethidium bromide (EB, Sigm a-Aldrich) 4 d after seeding. The cells cultured on the blend films w ereincubated in FDA/EB (5 mg mL^{-1}, 10 mg mL^{-1}, respectively) for 5 min at 37 ^{o}C and then washed twice in PBS (Sigma-Aldrich). Dead c ells were stained red due to the nuclear permeability of EB. Viable c ells, capable of converting the non-fluorescent FDA into fluorescein, were stained green. The surface images were obtained by using a con focal laser scanning microscopy (CLSM, Eclipse 90i, Nikon, Japan).

2.3. Results and Discussion

P3HT and the blend films with different weight ratios of P3HT/PHE MAAA = 75/25, 50/50, and 25/75 were used as an active layer of O TFT devices for determining their electrical properties. Output and tra nsfer curves of OTFTs with the blend films are shown in Figure 2.2 and the OTFT characteristics, such as the field-effect mobility (m), cur renton/off ratio (I_{on}/I_{off}), and threshold voltage (V_t) obtained from the transfer curve are briefly summarized in Table 2.1. The hole mobility value based on the P3HT film was observed to be 7.6×10^{-3} cm^2 V^{-1} s^{-1}, which is close to the other reported values prepared from P3HT [17]. The hole mobility values of OTFT devices prepared using the P3HT/PHEMAAA blend films were found to be only slightly smaller than that from P3HT film, despite the presence of the PHEMAAA in sulator.In particular, the value was maintained on the order of 10^{-3} ev en when the blend included 75 wt% PHEMAAA (25/75 blend). Since the hole mobility values were calculated using only the dielectric co nstant of the SiO_2 layer, without consideration of the much lower diel ectric constant of PHEMAAA, for all blends they are expected to be higher in experimental conditions than in theory. In addition, OTFT d evices based on P3HT/PHEMAAA blend films showed on–off current

ratios that are greater by two orders of magnitude for all samples, a nd theirthreshold voltages (V_t) were in the range of -2.9 to -6.1 V, c omparable to those of OTFT devices from P3HT blend systems report ed previously [18]. This result can be attributed to the formation of ef fective conductive networks of P3HT molecules, which can help to ge nerate charge transportation [24]. Also, this indicates the minimal influ ence of PHEMAAA on the OTFT properties caused by phase separati on between each polymer component. This could be correlated with o ther surface properties such as molecular orientation, morphology, and composition as discussed below.

The molecular orientation of each P3HT/PHEMAAA blend film was o bserved using grazing incidence wide-angle X-ray diffraction (GIWAX D) and compared with that of the P3HT film. It was reported that the OTFT devices fabricated from P3HT derivatives show high device performances when the P3HT has an edge-on structure with well-align ed alkyl side chains, because the π-π stacking direction is aligned with the charge transport direction in this configuration [25]. As shown in Figure 2.3, P3HT and the P3HT/PHEMAAA blend films all have edg e-on structures, primarily as a series of out-of-plane (100) reflections a re observed along with minor contributions of the face-on structures f

rom the π-π stacking peak at q = 1.67 $Å^{-1}$ in the out-of-plane directio n. The interlayer *d*-spacings calculated from the (100) peaks of P3HT and P3HT/PHEMAAA blend films are in the range of 16–17 Å and t heir π-π stacking distances are approximately 4.2 Å (Table 2.2), indicati ng that the P3HT molecules have a tightly packed lamellar structure with interdigitated side chains irrespective of the blend composition [2 6]. This result reveals that the amorphous PHEMAAA had no influen ce on the molecular orientation of P3HT, which is associated with th e favourable OTFT device performances of the P3HT/PHEMAAA blen d films. Thewell-oriented P3HT structures in the blends could be ascr ibed to the phase separation between the ordered and disordered poly mers in the blend [27], which was observed from the morphology stud ies in the next part.

Figure 2.4 shows the AFM topographical images of P3HT, PHEMAA A, and the blend surfaces according to the blend ratio. P3HT had a fl at surface (R_{rms} < 1 nm), while PHEMAAA had an extremely rough s urface with over 1 um-size of randomly distributed aggregates (R_{rms} = 70 nm). This is because PHEMAAA has a comparatively lower solub ility in MCB, present when the $CHCl_3$/MCB mixture was used for the film preparation. MCB was added to make edge-on structures for obta

ining good electrical performance as reported previously [22], though C HCl_3 is a good solvent for both P3HT and PHEMAAA. The R_{rms} val ues increased from 3.3 nm (75/25 blend) to 19.6 nm (25/75 blend) be cause the size of the islands increased according to the content of PH EMAAA as shown in the line profiles of Figure. 2.4, though these we re not as high as what was observed in PHEMAAA (70.1 nm). The p hase-separated structures of the polymer blends can be better understoo d by observing the surface structures obtained after selective dissolutio n of the P3HT fraction in the blends using MCB. Figure. 2.5 shows t hat theisland structures of the 75/25 and 50/50 blend surfaces become clearerby removal of the P3HT. Accordingly, the roughness value of the 75/25 blend surface increased from 3.3 nm to 9.1 nm and that of the 50/ 50 blend also increased from 12.9 nm to 15.1 nm. On the other hand, the 25/ 75 blend with less P3HT did not show any differences before and after the s olvent treatment. These results can be explained by a proposed model, whic h predicts the configuration of the blend domains according to the blend co mposition as displayed in Figure 2.6. When the P3HT content is relatively h igh (i.e. in the 75/25 and 50/50 blends), a large amount of P3HT domains m ight be located at the surface along with PHEMAAA domains. Therefore, th e removal of the P3HT domains on the blend surfaces results in a larger rou

ghness value by increasing the height of islands. However, the roughn ess value of the 25/75 blend remained almost constant, even after sel ective dissolution of the P3HT, as these domains were mainly located on the lower regions of the film, which are difficult for the etching s olvent to access. Due to the phase-separated structure of the blends, P 3HT can establish conductive networks with well-ordered lamellar stru ctures in the larger PHEMAAA matrix. The connective networks of P 3HT domain were clearly observed from inner parts of all the blend films by investigating SEM images obtained after selective dissolution of PHEMAAA domains (Figure 2.7).

For further verification of the phase-separated structures of the P3HT/ PHEMAAA blend films, XPS measurements were carried out, and the results were in good agreement with the AFM evidence. Surface com positions of the P3HT/PHEMAAA blend films were examined by com paring O/S ratios obtained from O_{1s} and S_{2p} core level XPS spectra a s shown in Figure 2.8a, since of the two materials only P3HT contai ns sulfur, while only PHEMAAA contains oxygen. The O_{1s} is compos ed of two peaks: a peak from the C=O moiety at 532.5 eV, and a p eak from the C–O moiety at 533.9 eV. In addition, the S_{2p} of the C –S moiety was measured at 163.1 and 164.3 eV. Figure 8b shows th

e O/S ratios of the P3HT/PHEMAAA blend films before and after di ssolution in MCB. Before the selective removal of P3HT domains, th e O/S ratios of the 75/25 and 50/50 blend surfaces are similar and s maller than those of 25/75 blend. This result suggests that the 75/25 and 50/50 blend surfaces are mainly occupied by the thiophene group s of P3HT, while in the case of 25/75 blend, a greater amount of P HEMAAA exists in the upper region of the film. After dissolution of the P3HT domains, the O/S ratios of all polymer surfaces increase du e to the increased proportion of PHEMAAA content. On the other ha nd, the relatively low value of the O/S ratio in the 25/75 blend surfa ce arises from the large amount of PHEMAAA covering the P3HT d omain on the surface before the solvent etching. These results could be well-correlated with the observations made in the previous part. Th ese compositional differences might be based on the clear phase-separ ation between P3HT and PHEMAAA with the formation of the differ ent domain size of each polymer part according to the blend composi tion. On the other hand, the influence of surface energy on the phase -separated structure of the blend films is considered to be marginal b ecause the surface energy of P3HT (34.3 mN m^{-1}) is quite lower tha n that of PHEMAAA (44.6 mN m^{-1}) as shown in Table 2.3; it has b

een reported that a polymer part with lower surface energy tends to migrate toward the top surface [28,29]. On the other hand, quite a fe w researchers suggested that the phase-separated structure of blends could be determined by various factors, such as solvent choice and polymer–substrate interaction besides surface energy of polymers [30,31].

To investigate the biocompatibility of the P3HT/PHEMAAA blend fil ms, both quantitative and qualitative tests were carried out using HDF s. First, neutral red assays were performed for 4 d to determine the v iability of cells cultured on P3HT, PHEMAAA, and the P3HT/PHEM AAA blend films. Since only live cells cultured on the samples can a bsorb the neutral red dye, cell viability results could be quantitatively obtained by measurement of the optical density. Figure 2.9 shows the viability of HDFs, which were cultured on P3HT, PHEMAAA, and th e P3HT/PHEMAAA blend films. Here, PHEMAAA was chosen as a positive control because the excellent biocompatibility of PHEMAAA has been fully demonstrated in the past [21]. Moreover, the poor viab ility of cells cultured on P3HT could be observed with optical micros copy (Figure 2.9a). It has been previously reported that unmodified P 3HT surfaces show poor cell adhesion [9]. Figure 2.9f shows that onl y 25 wt%of PHEMAAA is needed to drastically enhance the viability

of cells cultured on P3HT. Moreover, the significantly larger surface coverage of HDFs on the P3HT/PHEMAAA blend films supported the enhancement of cell viability owing to the presence of PHEMAAA domains (Figure 2.9e). In particular, the 25/75 blend film has the highest content of PHEMAAA among the blend ratios and exhibits almost same cell viability as that of PHEMAAA. The cytotoxicity of the P3HT/PHEMAAA blend films was also evaluated using a qualitative assay of live/dead cells, wherein live cells are stained green and the nuclei of dead cells are stained red. Figure 2.10 shows that most of the cells are alive with no apparent red signals from any of the blend films. This result indicates that none of the P3HT/PHEMAAA blend films shows any cytotoxic behavior on their surfaces, demonstrating their huge potential to be applied as implantable electronic devices. Furthermore, the effects of PHEMAAA content on the biocompatibility of the blend films are consistent with the results discussed for the neutral red assay; the CLSM images also show that increased PHEMAAA content in the blend solutions could improve the cell viability of the blend films. In particular, the surface of the 25/75 blend film is the most abundant in green-stained HDFs, comparable to that observed on PHEMAAA. Considering the results of both cell tests, the viability of cells cu

ltured on the P3HT/PHEMAAA blend films was found to increase wi th the addition of PHEMAAA. Since the surface (which comes in dir ect contact with the cell) is composed mostly of PHEMAAA, the cell s could be more active than when they were cultured on the surface of P3HT. In particular, the 25/75 blend has the highest PHEMAAA c ontent among all the blend films and shows biocompatibility compara ble to that of PHEMAAA. Additionally, the greater surface roughness could play a role in accelerating cell adhesion and proliferation, based on previous reports [21]

2.4. Conclusion

In conclusion, we successfully developed biocompatible semiconducting films by blending of a polymer semiconductor (P3HT) and a biocompatible polymer (PHEMAAA). All of the P3HT/PHEMAAA blend films having more than 25 wt% of P3HT showed stable OTFT performances comparable to those of P3HT, which indicates that efficient connective conductive networks could be formed in the blend films without a critical disturbance of PHEMAAA. The biocompatibility of P3HT can be highly enhanced by adding more than 25 wt% of PHEMAAA. In particular, the best cell-adhesion and viability were achieved with the addition of 75 wt% of PHEMAAA (25/75 blend), similar to that of PHEMAAA. Therefore, it is believed that the 25/75 blend is the preferable blend to obtain the best combination of electrical properties and biocompatibility, owing to the phase-separated structure and higher surface roughness.

2.5. References

[1] C. D. Dimitrakopoulos and P. R. Malenfant, Adv. Mater., 2002, 14, 99.

[2] M. Fadlallah, G. Billiot, et al., Solid-State Electron., 2007, 51, 1047.

[3] K. Fukuda, Y. Takeda, et al., Sci. Rep., 2014, 4, 3947.

[4] H. U. Khan, M. E. Roberts, et al., Chem. Mater., 2011, 23, 1946.

[5] P. Lin, F. Yan, et al., Adv. Mater., 2010, 22, 3655.

[6] G. Schwartz, B. C.-K. Tee, et al., Nat. Commun., 2013, 4, 1859.

[7] E. Bystrenova, M. Jelitai, et al., Adv. Funct. Mater., 2008, 18, 1751.

[8] D. H. Kim, S. M. Richardson-Burns, et al., Adv. Funct. Mater., 2007, 17, 79.

[9] G. Scarpa, A. L. Idzko, et al., Macromol. Biosci., 2010, 10, 378.

[10] D. Mawad, E. Stewart, et al., Adv. Funct. Mater., 2012, 22, 2692.

[11] J. A. Goding, A. D. Gilmour, et al., J. Mater. Chem. B, 2015, 3, 5058.

[12] X. Cui, V. A. Lee, et al., J. Biomed. Mater. Res., 2001, 56, 261.

[13] J.-C. Lin, W.-Y. Lee, et al., J. Mater. Chem., 2012, 22, 14682.

[14] M. M. P. Madrigal, M. I. Giannotti, et al., Polym. Chem., 2013,

4, 568.

[15] M. M. P´erez-Madrigal, E. Armelin, et al., Polym. Chem., 2012, 3, 979.

[16] A. Babel and S. A. Jenekhe, Macromolecules, 2004, 37, 9835.

[17] L. Qiu, W. H. Lee, et al., Adv. Mater., 2009, 21, 1349.

[18] X. Wang, W. H. Lee, et al., J. Mater. Chem. C, 2013, 1, 3989.

[19] R. J. Kline, M. D. McGehee, et al., Macromolecules, 2005, 38, 3312.

[20] E. Armelin, A. L. Gomes, et al., J. Mater. Chem., 2012, 22, 585.

[21] E. H. Sohn, J. Ahn, et al., Macromol. Biosci., 2012, 12, 211.

[22] K. Zhao, Z. Ding, et al., Macromol. Rapid Commun., 2010, 31, 532.

[23] D.K. Owens, R.C. Wendt, et al., J. Appl. Polym. Sci., 1969, 13, 1741.

[24] S. Goffri, C. M¨uller, et al., Nat. Mater., 2006, 5, 950.

[25] R. Singh, J. S. Meena, et al., RSC Adv., 2014, 4, 29383.

[26] B. S. Ong, Y. Wu, et al., J. Am. Chem. Soc., 2004, 126, 3378.

[27] L. Qiu, J. A. Lim, et al., Adv. Mater., 2008, 20, 1141.

[28] S. Y. Heriot, R. A. Jones, et al., Nat. Mater., 2005, 4, 782.

[29] A. C. Arias, et al., Appl. Phys. Lett., 2002, 80, 1695.

[30] E. H. Sohn, B. G. Kim, et al., J. Colloid Interface Sci., 2011,

354, 650.

[31] K. Tanaka, K. Takahara, et al., Macromolecules, 1996, 29, 3232.

Table 2.1. Average field-effect mobilities of the OTFT devices prepared from the polymer films.

Polymer films	**P3HT**	**P3HT/PHEMAAA (wt%)**		
		75/25	**50/50**	**25/75**
Mobility, μ ($cm^2 \cdot V^{-1} \cdot s^{-1}$)	7.6×10^{-3}	4.4×10^{-3}	3.9×10^{-3}	3.2×10^{-3}
I_{on}/I_{off}	8.2×10^{2}	9.0×10^{2}	1.4×10^{2}	3.4×10^{2}
V_t	-2.9	-2.6	-6.1	-3.9

Table 2.2. The *d*-spacings of P3HT/PHEMAAA blend films determined from GIWAXD measurements.

d - spacing	P3HT	P3HT/PHEMAAA (wt%)		
		75/25	50/50	25/75
Lamellar spacing	16.3 Å	16.8 Å	16.3 Å	16.8 Å
π-π spacing	4.2 Å			

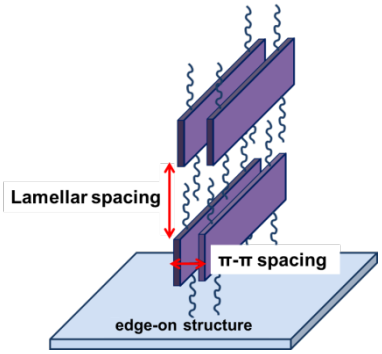

Table 2.3. The contact angles of deionized water and DIM measured on the P3HT and PHEMAAA films and the surface energies of the polymers.

Sample	Contact angles [degrees][a]		Surface energy (mN/m)[b]
	DI-water	Diiodomethane (DIM)	
P3HT	104.0 (0.8)	49.9 (1.2)	34.3
PHEMAAA	72.7 (1.1)	36.7 (0.9)	44.6

[a]Standard deviations are given in parentheses. [b]Calculated using Owens-Wendt-Rable-Kaelble method.

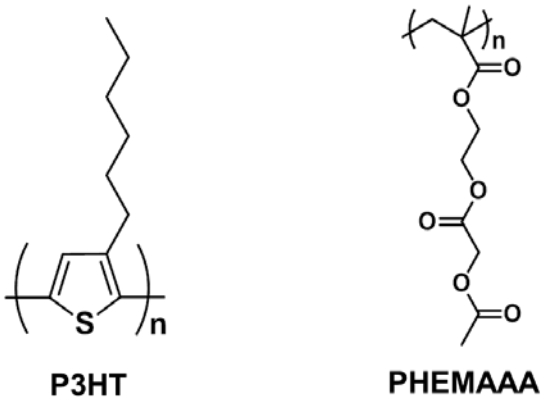

Figure 2.1. Chemical structures of P3HT and PHEMAAA.

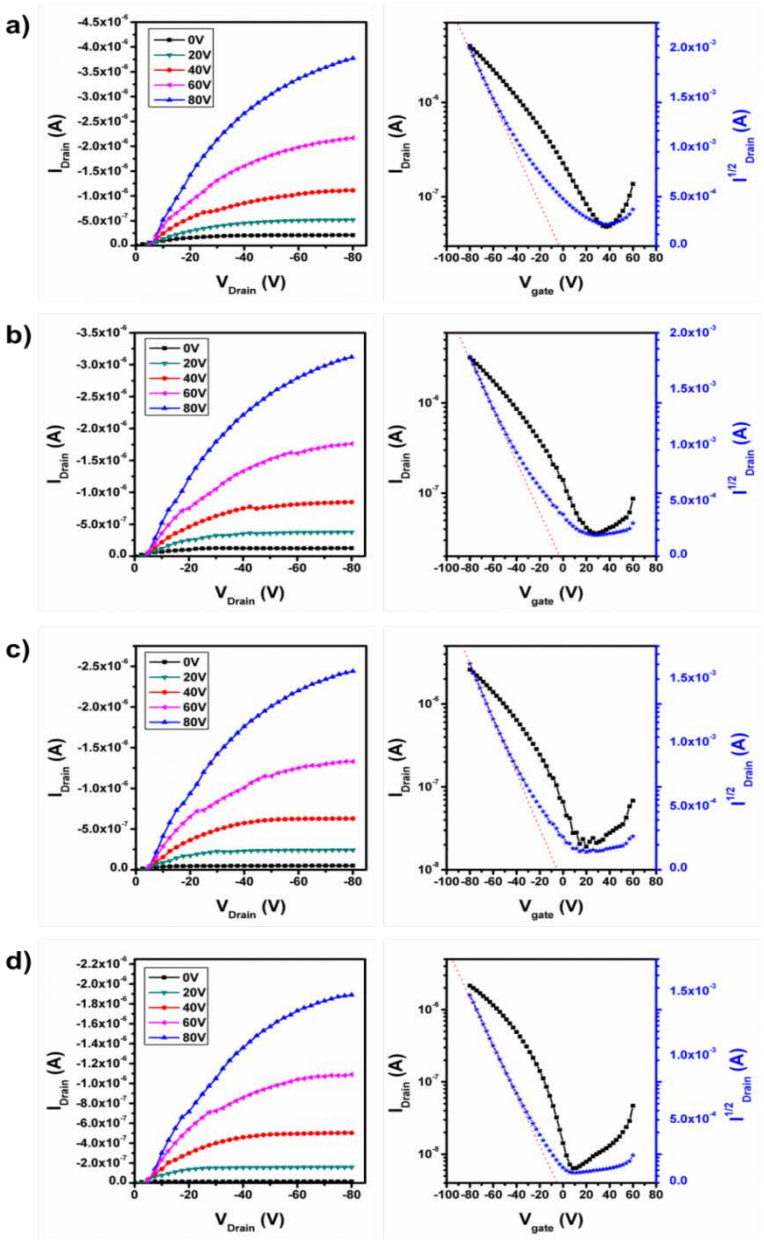

Figure 2.2. Output and transfer curves obtained from a) P3HT, b) 75/25 blend, c) 50/50 blend, and d) 25/75 blend.

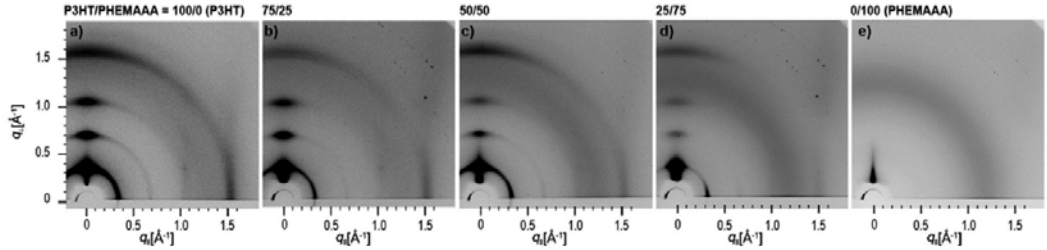

Figure 2.3. GIWAXD 2D patterns of a) P3HT, b) 75/25 blend, c) 50/50 blend, d) 25/75 blend, and e) PHEMAAA films.

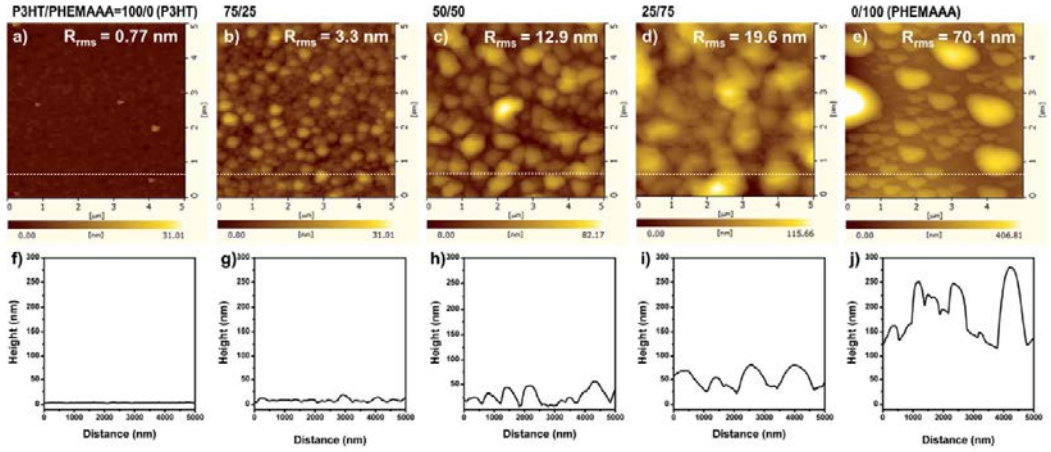

Figure 2.4. AFM height images (5 um × 5 um) of a) P3HT, b) 75/25 blend, c) 50/50 blend, d) 25/75 blend, and e) PHEMAAA films, and f–j) corresponding line profiles.

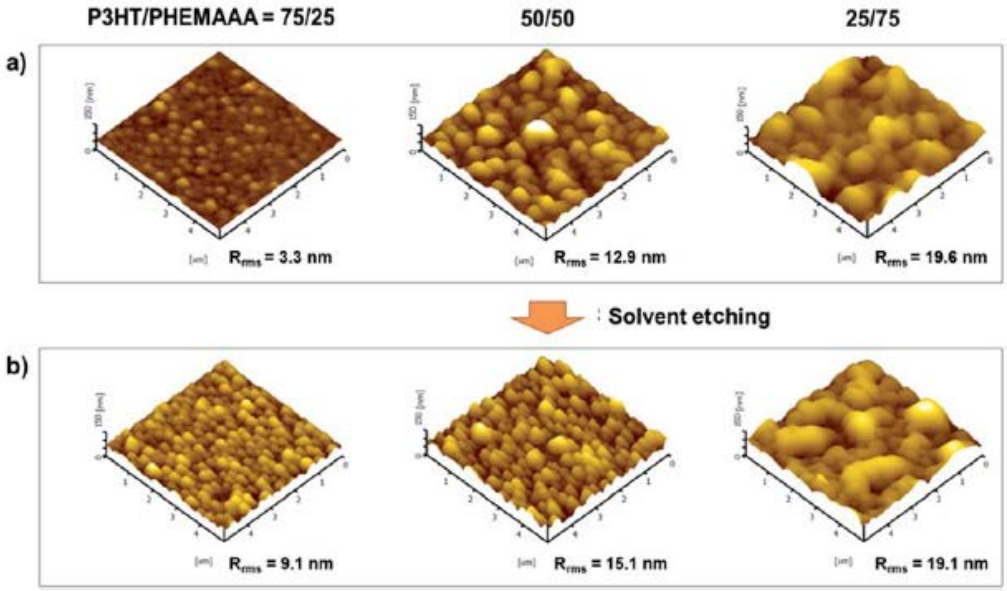

Figure 2.5. AFM topographic 3D images of the 75/25 blend, 50/50 blend, and 25/75 blend surfaces a) before and b) after selective dissolution of P3HT part with MCB.

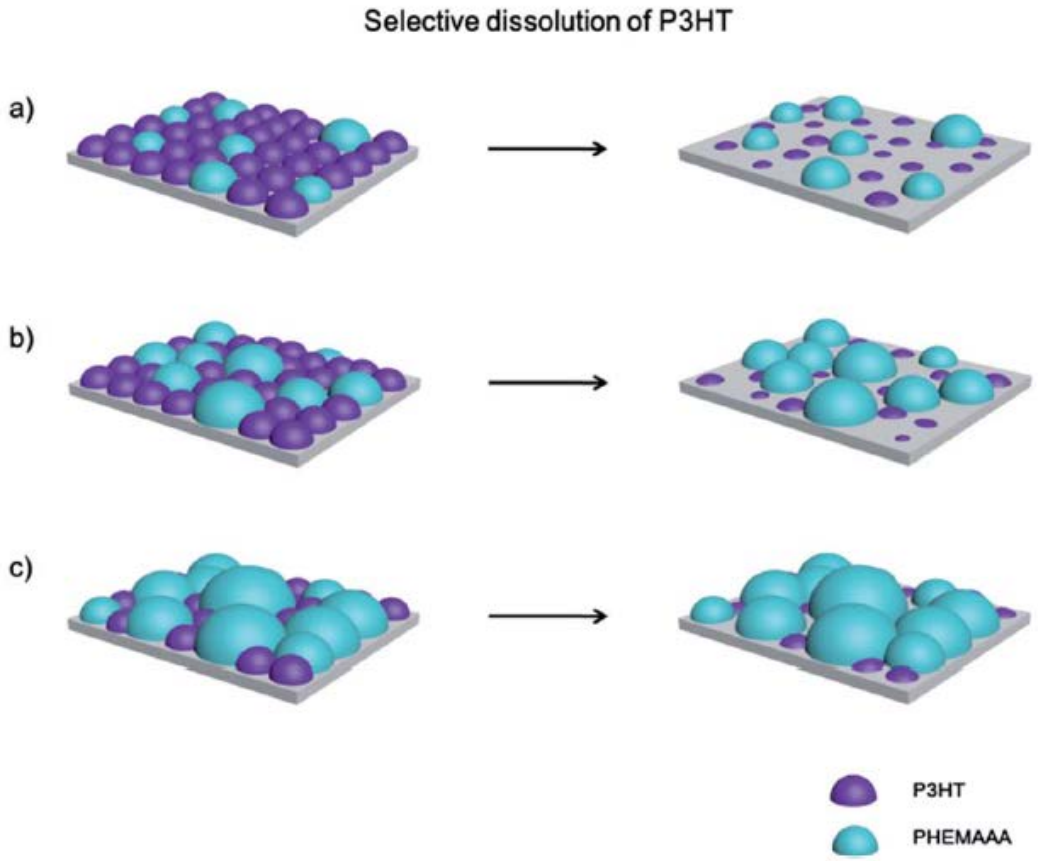

Figure 2.6. A schematic diagram explaining the change of surface morphology before and after selective dissolution of P3HT according to blend composition; a) 75/25 blend, b) 50/50 blend, and c) 25/75 blend.

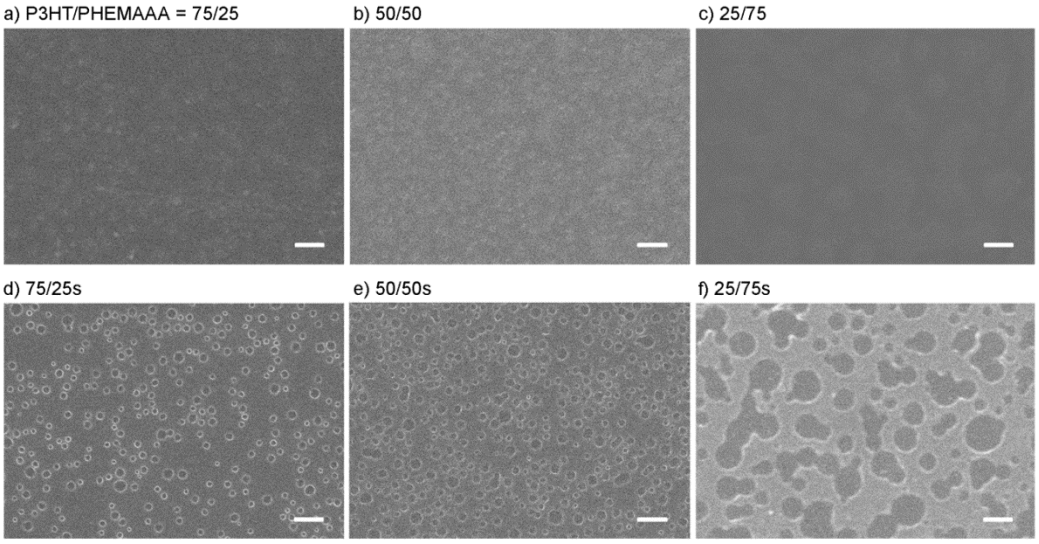

Figure 2.7. FE-SEM images of P3HT/PHEMAAA blend films a)-c) before and d)-f) after selective dissolution of PHEMAAA part using THF. (scale bar = 1 um) The connective networks of P3HT domain were observed from all blend surfaces by measuring the film morphologies obtained after selective dissolution of PHEMAAA.

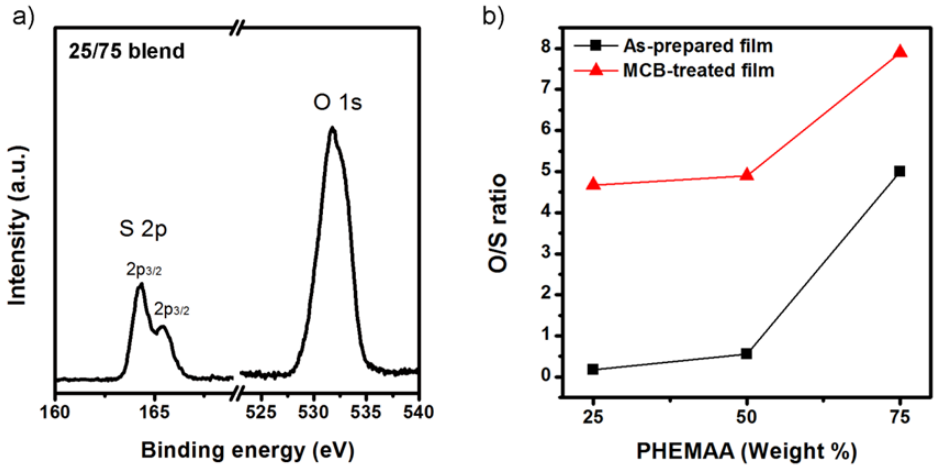

Figure 2.8. The representative XPS S_{2p} and O_{1s} core level spectra on the surfaces of a) 25/75 blend and b) O/S ratios of P3HT/PHEMAAA blend films before (black square line) and after MCB treatment (red triangle line).

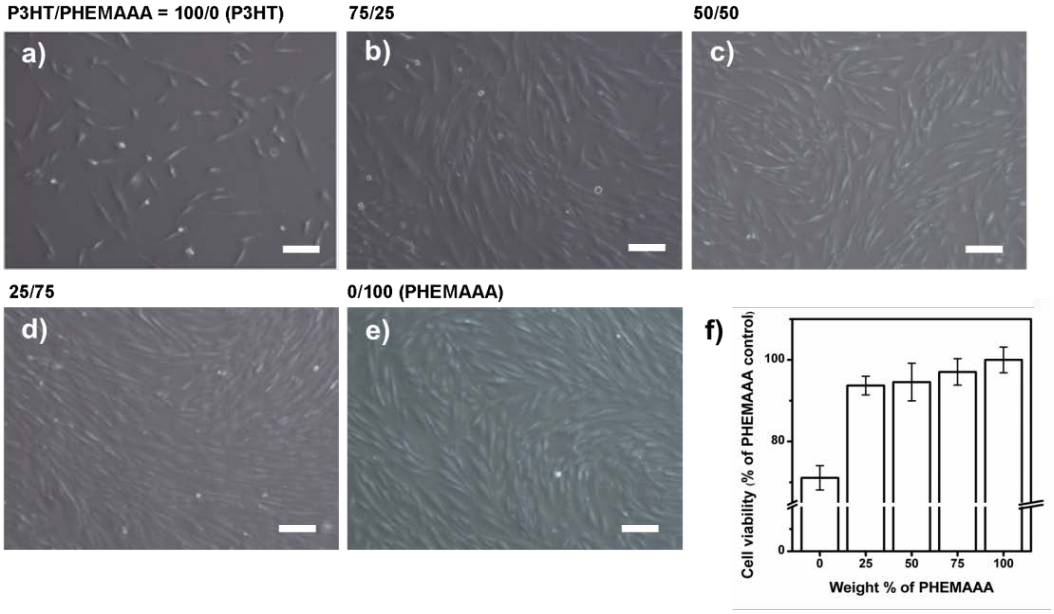

Figure 2.9. Representative optical microscopy images of HDFs cultured for 4 days on a) P3HT, b) 75/25 blend, c) 50/50 blend, d) 25/75 blend, e) PHEMAAA films, and f) the quantitative results (scale bar = 100 um).

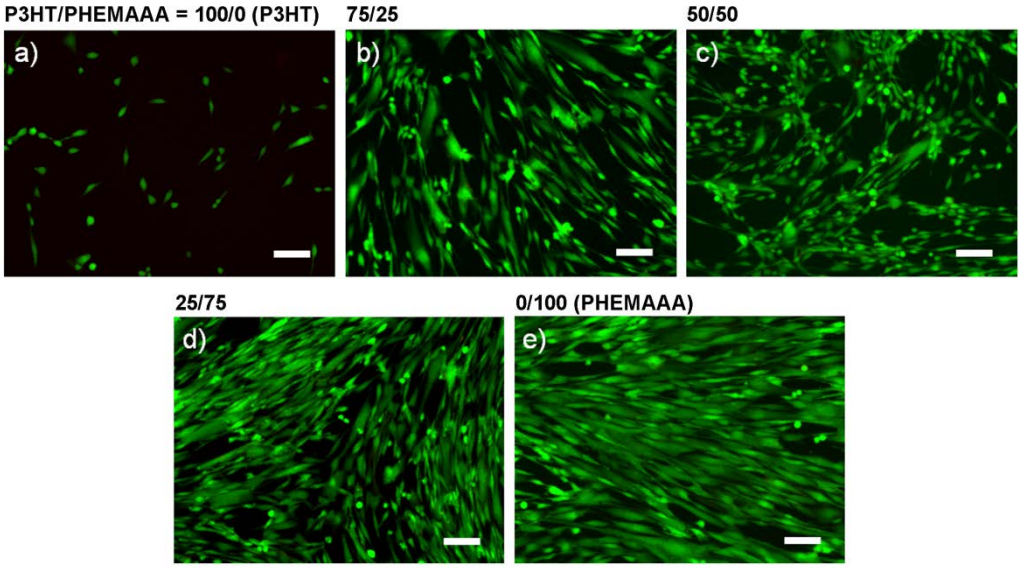

Figure 2.10. CLSM images presenting FDA/EB staining on HDFs cultured for 4 d on a) P3HT, b) 75/25 blend, c) 50/50 blend, d) 25/75 blend, and e) PHEMAAA films (scale bar = 100 um).

Chapter 3

Natural Resource-Based Polymeric Dielectric for Flexible OTFT System

3.1. Introduction

Organic field-effect transistors (OFETs) have been applied to various optical and electrical devices, such as active matrix displays, radio-frequency identification tags, and sensing applications, due to several advantages of easy fabrication process and low-cost mass production capability over the conventional inorganic FETs [1-3]. Especially, OFET based-sensors with high sensitivity are considered to be a strong candidate for biomedical, disposable, and miniaturized diagnostics to perform the drug screening and toxicity test [4-5]. The emerging biomedical applications widely stimulate the need for finding organic electronic materials that have both sustainable electronic properties and unharmful effects on biological function, to develop safe, nontoxic, and ecologically-sustainable organic electronics. Several natural resource-based materials, including dyes (e.g., indigo and beta-carotene) as well as deoxyribonucleic acid, paper, silk, shellac, cellulose, and chicken albumen have been recently utilized in applications ranging from semiconductors to gate dielectrics in the OFETs [6-16]. Although natural resource-based materials have been introduced as ideal organic materials in ‘green electronics’, there remain critical limitations that inhibit their stable operation in organic electronics. In particular, applications of natural resources as dielectric materials in

OFETs have some intrinsic problems that must be solved. First, natural resources generally possess hydrophilic properties, which are detrimental to OFET devices due to their water sensitivity [8]. The high surface energy of natural resources also results in difficulties in coating solution-processed polymeric semiconductors onto their surfaces [17]. Moreover, natural resource-based gate dielectrics are likely to suffer from high hysteresis, which leads to unstable OFET device operation [18]. Cardanol is a renewable natural resource that is obtained from cashew nut shell liquid. Its specific chemical structure, which has a phenolic moiety and a C15 unsaturated alkyl chain, leads to several advantages such as its bactericidal, hydrophobic, and self-crosslinking properties [19-20]. A few cardanol-based polymers have been previously synthesized and utilized as excellent coating materials [20-21]. We utilized cardanol-based poly(2-hydroxy-3-cardanylpropyl methacrylate) (PHCPM) as a gate dielectric in OFETs on flexible substrates. PHCPM has good surface properties, appropriate gate dielectric characteristics, and good compatibility with solution-processed semiconducting polymers (e.g., poly[2,5-bis(3-dodecylthiophen-2-yl)thieno [3,2-b]thiophene] (PBTTT)). In this study, the electrical properties of an OFET that was prepared with natural resource-based PHCPM as a dielectric

layer and solution-processed PBTTT as a semiconducting layer were investigated on rigid or flexible substrates.

3.2. Experimental

Top-contact PBTTT-OFET devices were fabricated with solution-processed PBTTT on PHCPM films, which were coated onto rigid ITO-glass and flexible ITO-PET (polyethylene terephthalate) substrates. PBTTT (Mw = 40,000-80,000 g/mol) was purchased from Sigma-Aldrich and PHCPM (Mw = 8,200 g/mol) was synthesized according to previous reports [21]. All substrates were cleaned with ethanol and deionized water using ultra-sonication for 10 min. A 10 wt% PHCPM solution in tetrahydrofuran (THF) was spin-coated onto the substrates at 3000 rpm for 60 s, followed by a thermal treatment at 180 ^{o}C for 5 h. The thermal treatment conditions were determined based on previous DSC results [21]. The PBTTT solution (10 mg/mL) in 1,2-dichlorobenzene was directly coated onto the PHCPM layer by spin-coating at 2000 rpm for 60 s, followed by annealing at 180 ^{o}C for 30 min. The PBTTT-OFET device was then completed by thermally evaporating 50-nm-thick source and drain gold electrodes on top of the PBTTT active layer, creating transistors with a channel length (L) of 20-100

um and a width (W) of 0.5-1 mm. Numerical differentiation of the I_{DS} with respect to the V_{GS} allows the field-effect transistor mobility (μ) to be calculated in the saturation regime using Equation (3.1). In this equation, W, L, C_i, and V_T are the channel width, channel length, capacitance per unit area of the dielectric layer, and threshold voltage, respectively. The field-effect mobility values in the saturation region were calculated from the slope of the square root of the drain-source current as a function of the gate-source voltage, i.e., the $|I_{Dsat}|^{1/2}$ versus V_g plot.

$$I_{Dsat} = \frac{WC_i}{2L}\mu(V_{GS} - V_T)^2 \qquad (3.1)$$

The reaction of the cross-linked PHCPM film was confirmed by using an attenuated total reflection method with a Jasco-6000 Fourier transform infrared spectrometer (FTIR). The surface morphology of the PHCPM film was studied using an atomic force microscope (AFM, Park System XE-70). The contact angles of deionized water and diiodomethane (DIM) were measured at room temperature using a Kruss DSA 10 contact angle analyzer. The Owens-Wendt-Rabel-Kaelble (OWRK) method was used to calculate the surface energy of the polymer film [22]. Grazing incidence wide-angle X-ray diffraction (GIWAXD) was performed using a high-power X-ray beam (photon flux = 10^{11} photons s^{-1} $mrad^{-1}$ per 0.1%, beam size ≤ 0.5 mm2)

from a synchrotron radiation source (3C beamline, Pohang Accelerator Laboratory, Korea) at l = 1.24 Å. In order to determine the capacitance and leakage current of the PHCPM film, metal-insulator-metal (MIM) capacitor structures were prepared by deposition of an Al electrode on the 830 nm thick PHCPM film-coated Si wafer using a thermal evaporator. The thickness and active area of Al electrode in the MIM device were 100 nm and 0.65 mm2, respectively. The frequency dependence of the capacitance and leakage current measurements was evaluated using an Agilent 4284A LCR meter and 4156C semiconductor parameter analyzer, respectively. The electrical properties of the PBTTT-OFET were measured using an Agilent 4156C semiconductor parameter analyzer under ambient conditions.

3.3. Results and Discussion

Poly(2-hydroxy-3-cardanylpropyl methacrylate) (PHCPM) was developed using a natural resource, cardanol, which can be obtained from cashew nut shell liquid (Figure 3.1). PHCPM was synthesized by free-radical polymerization of the HCPM monomer, which was prepared by the reaction of cardanol and glycidyl methacrylate. The detailed procedure of the synthesis of PHCPM was reported in our previous work [21]. Since PHCPM can be cross-linked through the unsaturated alkyl groups at the side

chain, it represents a good candidate for use as the gate dielectric of OFETs in order to avoid unstable device operation caused by ionic migration [23-24]. After the PHCPM film was spin-coated from 10 wt% of the PHCPM solution, cross-linking of the unsaturated alkyl groups in PHCPM was induced by a thermal treatment at 180 ^{o}C for 5 h. Crosslinking of the unsaturated alkyl side chains can be confirmed by analyzing the FTIR spectra (Figure 3.2), which shows the disappearance of the C-H stretching vibration peak of the alkene group at 3010 cm^{-1}. In order to be used as a gate dielectric for stable OFET devices, PHCPM should meet various film properties. These include a low surface roughness, low surface energy, good dielectric constant (k), and low leakage current. The surface properties of the PHCPM film were investigated using water contact angle and surface roughness measurements. The surface of the PHCPM film was found to be hydrophobic (Table 3.1) and had a lower surface energy (36.7 mN/m) than SiO2 (61.4 mN/m) and HMDS-treated SiO_2 (43.6 mN/m) [25]. These properties should be advantageous for the preparation of water-sensitive OFET devices. The root-mean-square (RMS) roughness of the cross-linked PHCPM film was measured using AFM (Figure 3.3); this was determined to be 0.37 nm. The RMS roughness value is similar to those of other natural resource-based dielectrics such as silk fibroin, cellulose, and chicken

albumin [9-11]. Such surface properties of the PHCPM film with cross-linked side chains are sufficient for use as the gate dielectric of OFETs prepared with solution-processed semiconducting polymers [11,25]. The dielectric constant of PHCPM was determined by performing capacitance measurements with the MIM capacitor structure. Although natural resource-based gate dielectrics often suffer from serious frequency dependency of the capacitance, the PHCPM film exhibits very stable capacitance characteristics, irrespective of frequency variations. It is clearly shown in Figure 3.4a that the capacitance values slowly decrease with increasing frequency from 4.2 nF/cm^2 at 1 KHz to 3.7 nF/cm^2 at 1 MHz. The dielectric constant of the PHCPM film was derived from the capacitance values using Equation (3.2):

$$k = Cd/\varepsilon_0 A \quad (3.2)$$

Here, C is the capacitance, d is the thickness of the film, ε_0 is the permittivity of a vacuum, and A is the area of the OFET device. As shown in the inset of Figure 3.4a, the dielectric constant decreases with increasing frequency from 3.9 at 1 KHz to 3.0 at 1 MHz; this value is comparable to that of silicon oxide [7]. Because the values of the capacitance and dielectric constant do not change with the frequency, it is obvious that no ionic

impurities are included in the PHCPM film [26]. The leakage current of the PHCPM dielectric film was evaluated using the MIM capacitor structure. Fig. 3.4b shows that the leakage current density increases with the voltage up to 1.0×10^{-6} A/cm^2, without breakdown, at less than 80 V. This is an acceptable level for OFET device operation [27-28]. The observed stability of the leakage current may be due to the thermally cross-linked side chain structure of the PHCPM film; this is the case because the leakage current of the dielectric can be reduced in the network structure [29]. Therefore, due to its surface properties and the dielectric characteristics of the film, PCHPM is worth considering as a gate dielectric for OFETs. As illustrated in the OFET device diagram of Fig. 3.1, PHCPM was coated as a gate dielectric on a rigid substrate of ITO-glass. On top of the PHCPM film, a solution-processed semiconducting polymer (i.e., PBTTT) was spin-coated as a p-type semiconductor. Since the PHCPM film was already thermally cross-linked, the PBTTT solution could not deteriorate the underlying PHCPM film during the coating process. Poor compatibility between solution-processed semiconductors and dielectrics can readily occur and cause OFET device degradation [17]. However, solution-processed PBTTT seems to be highly compatible with the PHCPM film due to the film's smoothness and low surface energy characteristics. The GIWAXD results confirmed that

PBTTT is well-grown on the surface of the PHCPM film. The halo peak of the amorphous PHCPM film and the concentrated lamellar-stacking peaks (100, 200, 300) at q = 0.28 $Å^{-1}$ along the vertical direction from the crystalline PBTTT film can be found in Figure 3.5 The GIWAXD peaks indicate the edge-on structure of PBTTT against the film substrate. This structure is preferential for charge transport because lamellar stacking is directed perpendicularly to the substrate [30]. Figure 3.6a shows the output characteristics of the PBTTT-OFET with the PHCPM dielectric film on a rigid ITO-glass substrate. The output characteristic curves of the PBTTT-OFET show good pinch-off and current saturation features. The saturated mobility values were obtained from the transfer characteristics and are shown in Figure 3.6b. The device performance, including the output and transfer characteristics, was obtained at ambient conditions. The mobility value of the PBTTT-OFET with the PHCPM dielectric was derived from the transfer curve and was determined to be 3.1×10^{-2} cm^2/Vs. This mobility value is slightly better than the previously reported values obtained for untreated silicon oxide-based OFET devices [31]. This high mobility value can be attributed to the good surface and dielectric characteristics of the PHCPM film. For the application of the PHCPM gate dielectric in a flexible OTFT device system, PHCPM was coated on a flexible ITO-coated

PET film with a thickness of 125 um. The device geometry of the flexible OFET is identical to that of rigid one with the glass substrate. In and out bending of the flexible device was repeated 100 times. All of the output characteristics were measured in the film bending state with a radius of 15 mm, which corresponds to the bending tensile strain of 0.42%. A similar bending work has been reported for a flexible OTFT with 60 um thick poly(ethylenenaphthalate) (PET) film whose tensile strain becomes 1.5% [32]. In addition, the flexible OFET generally suffers from an increased leakage current after bending, leading to low device performance [11]. In the case of the flexible OFET with PHCPM, however, the device performance is maintained without deterioration, even in the bending state after being bent 100 times. The flexible OFET still exhibits excellent device performance that is similar to the OFET with the rigid substrate. As seen in Figure 3.7, the mobility value and on/off ratio of the flexible OFET were found to be 2.0×10^{-2} and 1.2×10^{3}, respectively, which are almost identical to those obtained in the rigid ITO-glass substrate OFET. Furthermore, the hysteresis of the output and transfer characteristics was not observed during 10 cycle operations. This observation suggests that the PBTTT-OFET device with the PHCPM dielectric film on a flexible ITO-PET substrate can withstand, even though strain levels of more than 0.42 %

(bending radius under 15 mm) are repeatedly applied to them up to 100 times. It is considered that the thermally cross-linked PHCPM film as a dielectric material is mechanically stable without the impurity ion intrusion [23-24]. Therefore, it was demonstrated that the flexible OFET with the solution-processed PBTTT semiconducting polymer and the cardanol-based PHCPM dielectric exhibited a high mobility value and reliable performance, even in the bending state, without significant hysteresis.

3.4. Conclusion

Natural resource-based PHCPM was utilized as the gate dielectric of an OFET with solution-processed PBTTT as the semiconducting material. The gate dielectric properties of the thermally cross-linked PHCPM film were investigated by measuring the surface properties, capacitances, and leakage currents. It was found that the PHCPM film had a low surface roughness, a hydrophobic surface, a high dielectric constant, and a low leakage current. The electrical properties of the solution-processed PBTTT-OFET prepared with PHCPM as the gate dielectric exhibited a slightly higher mobility than an untreated SiO2 gate dielectric. It was clearly shown that the PHCPM dielectric was well suited for use in a solution-processed flexible OFET system. The PBTTT-OFET with the PCHPM dielectric on a flexible ITO-PET substrate showed reliable performance with a high mobility and on-off ratio, even in the bending state, without any hysteresis.

3.5. References

[1] D. Christos, P.R.L. Malenfant, Adv. Mater. 14 (2002) 99-117.

[2] M. Fadlallah, G. Billiot, W. Eccleston, D. Barclay, Solid-State Electron. 51 (2007) 1047-1051.

[3] K. Fukuda, Y. Takeda, M. Mizukami, D. Kumaki, S. Tokito, Sci. Rep. 4 (2014) 3947.

[4] P. Lin, F. Yan, Adv. Mater. 24 (2012) 34-51.

[5] G. Schwartz, B.C.-K. Tee, J. Mei, A.L. Appleton, D.H. Kim, H. Wang, Z. Bao, Nat. Commun. 4 (2013) 1859.

[6] M. Irimia-Vladu, Chem. Soc. Rev. 43 (2014) 588-610.

[7] M. Irimia-Vladu, P.A. Troshin, M. Reisinger, L. Shmygleva, Y. Kanbur, G. Schwabegger, M. Bodea, R. Schw€odiauer, A. Mumyatov, J.W. Fergus, V.F. Razumov, N.S. Sariciftci, S. Bauer, Adv. Funct. Mater. 20 (2010) 4069-4076.

[8] C. Yumusak, T.B. Singh, N.S. Sariciftci, J.G. Grote, Appl. Phys. Lett. 95 (2009) 263304-263307.

[9] C.H. Wang, C.Y. Hsieh, J.C. Hwang, Adv. Mater. 23 (2010) 1630-1634.

[10] A. Petritz, A. Wolfberger, A. Fian, T. Griesser, M. Irimia-Vladu, B. Stadlober,

Adv. Mater. 27 (2015) 7645-7656.

[11] J.W. Chang, C.G. Wang, C.Y. Huang, T.D. Tsai, T.F. Guo, T.C. Wen, Adv. Mater. 23 (2011) 4077-4081.

[12] M. Irimia-Vladu, E.D. Glowacki, G. Schwabegger, L. Leonat, H.Z. Akpinar, H. Sitter, S. Bauer, Green Chem. 15 (2013) 1473-1476.

[13] F. Eder, H. Klauk, M. Halik, U. Zschieschang, G. Schmid, C. Dehm, Appl. Phys. Lett. 84 (2004) 2673-2675.

[14] U. Zschieschang, T. Yamamoto, K. Takimiya, H. Kuwabara, M. Ikeda, T. Sekitani, T. Someya, H. Klauk, Adv. Mater. 23 (2011) 654-658.

[15] D. Tobj€ork, R. €Osterbacka, Adv. Mater. 23 (2011) 1935-1961.

[16] A. Hübler, B. Trnovec, T. Zillger, M. Ali, N. Wetzold, M. Mingebach, A. Wagenpfahl, C. Deibel, V. Dyakonov, Adv. Energy Mater. 1 (2011) 1018-1022.

[17] R. Hamilton, J. Smith, S. Ogier, M. Heeney, J.E. Anthony, I. McCulloch, J. Veres, D.D.C. Bradley, T.D. Anthopoulos, Adv. Mater. 21 (2009) 1166-1171.

[18] B. Singh, N.S. Sariciftci, J.G. Grote, F.K. Hopkins, J. Appl. Phys. 100 (2006) 24514-24517.

[19] A. Kumar, P.K. Vemula, P.M. Ajayan, G. John, Nat. Mater. 7 (2008) 236-241.

[20] D.G. Kim, H. Kang, Y.S. Choi, S. Han, J.C. Lee, Polym. Chem. 4 (2013) 5065-5073.

[21] Y.S. Choi, K.H. Kim, D.G. Kim, H.J. Kim, S.H. Cha, J.C. Lee, RSC Adv. 4 (2014) 41195-41203.

[22] D.K. Owens, R.C. Wendt, J. Appl. Polym. Sci. 13 (1969) 1741-1747.

[23] M.E. Roberts, N. Queralto, S.C. Mannsfeld, B.N. Reinecke, W. Knoll, Z. Bao, Chem. Mater. 21 (2009) 2292-2299.

[24] Y.S. Kim, K.H. Jung, U.R. Lee, K.H. Kim, M.H. Hoang, J.I. Jin, D.H. Choi, Appl. Phys. Lett. 96 (2010) 103307.

[25] S.C. Lim, S.H. Kim, J.H. Lee, M.K. Kim, T. Zyung, Synth. Met. 148 (2005) 75-79.

[26] J. Veres, S. Ogier, G. Lloyd, D. De Leeuw, Chem. Mater. 16 (2004) 4543-4555.

[27] L.L. Chua, P.K. Ho, H. Sirringhaus, R.H. Friend, Appl. Phys. Lett. 84 (2004) 3400-3402.

[28] M.H. Yoon, H. Yan, A. Facchetti, T.J. Marks, J. Am. Chem. Soc. 127 (2005) 10388-10395.

[29] S.H. Kim, S.Y. Yang, K. Shin, H. Jeon, J.W. Lee, K.P. Hong, C.E. Park, Appl. Phys. Lett. 89 (2006) 183516.

[30] R. Singh, J.S. Meena, Y.C. Chang, C.S. Wu, F.H. Ko, RSC Adv. 4 (2014) 29383-29428.

[31] J.W. Bae, K. Song, Org. Electron. 30 (2016) 143-148.

[32] T. Someya, T. Sekitani, S. Iba, Y. Kato, H. Kawaguchi, T. Sakurai, Proc. Natl. Acad. Sci. USA 101 (2004) 9966-9970.

Table 3.1. The contact angles of deionized water and diiodomethane measured on the PHCPM film and the derived surface energy.

Sample	Contact angle [degrees][a]		Surface energy (mN/m)[b]
	DI water	Diiodomethane	
PHCPM	91.0 (1.2)	44.6 (0.8)	36.7

[a] Standard deviations are given in parentheses. [b] Calculated using the Owens-Wendt-Rable-Kaelble method.

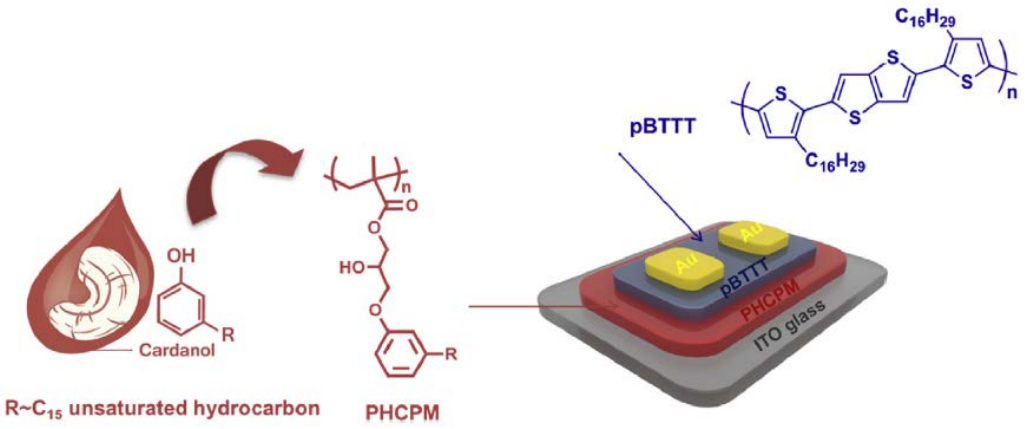

Figure 3.1. OFET device geometry with the chemical structures of PHCPM and PBTTT.

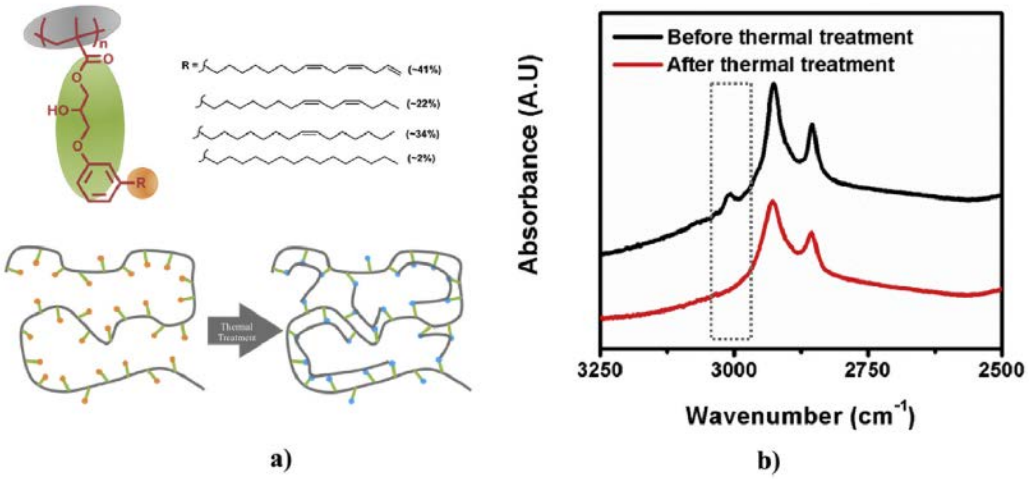

Figure 3.2. a) Schematic illustration of thermally crosslinked PHPCM and b) FTIR spectra of C-H stretching region of PHCPM films.

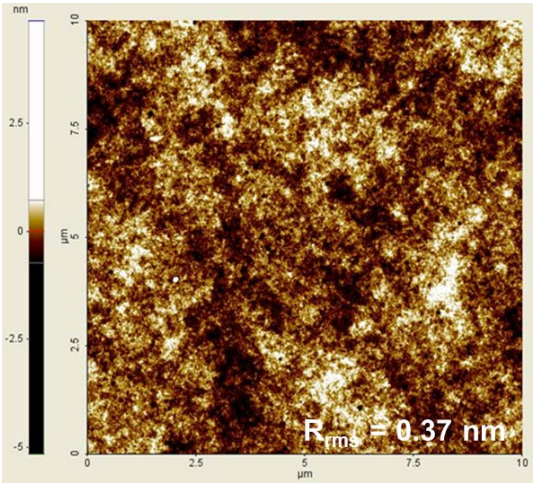

Figure 3.3. AFM height image (10 **u**m × 10um) of the PHCPM film**.**

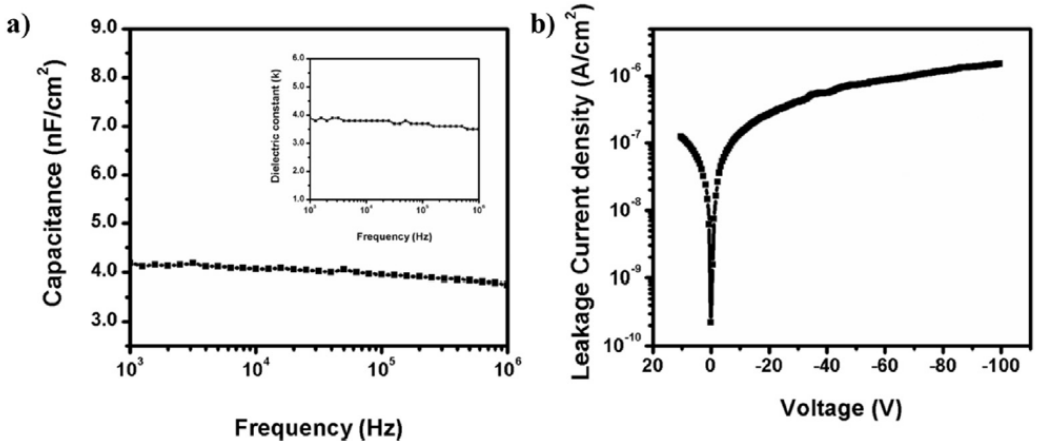

Figure 3.4. a) Capacitance-frequency and b) leakage current density-voltage characteristics of the PHCPM film. The dielectric constant dependency on the frequency is shown in the inset of a).

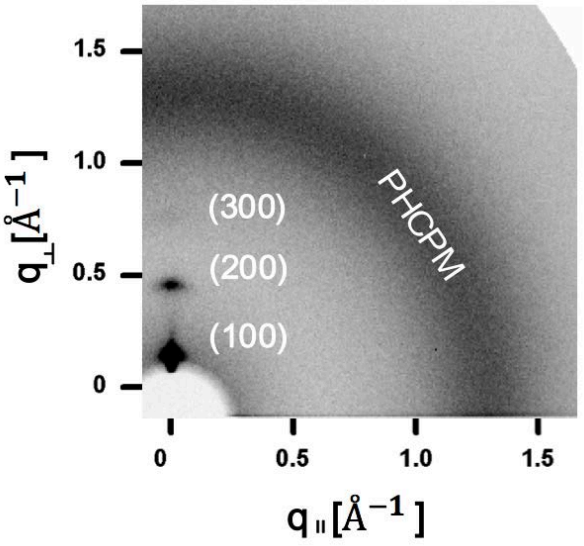

Figure 3.5. GIWAXD 2D pattern of the PHCPM film.

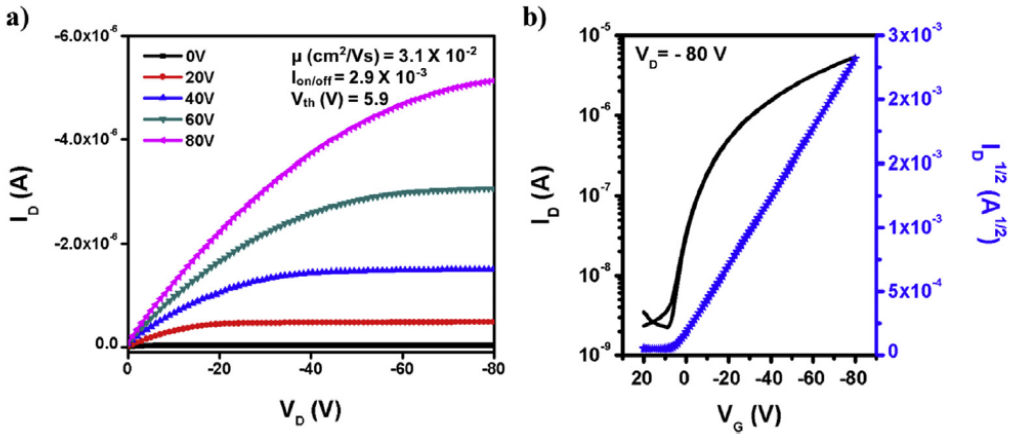

Figure 3.6. a) Output curves and b) Transfer curves obtained from PBTTT-OFET devices with the PHCPM gate dielectric.

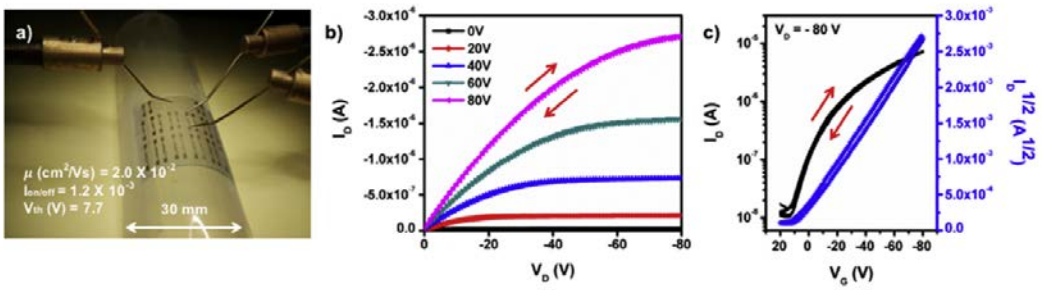

Figure 3.7. a) A photograph of the flexible PBTTT-OFET device with the P HCPM gate dielectric. b) Output curves and c) Transfer curves ofthe flexib le PBTTT-OFET device obtained in the bending state with a radius of 15 mm.

Chapter 4

Biocompatible Vitrimer Film

for 3D Hierarchical Scaffold Application

4.1. Introduction

The design and fabrication of three-dimensional (3D) scaffolds, capable of providing physiological environments that can support and grow the cells into specific tissues and ultimately organs, have been the main focus of tissue engineering (TE) for the last two decades.1 In addition to biocompatibility and tissue-like mechanical properties of the scaffold materials, controlling the scaffold architectures to mimic the extracellular matrix (ECM) of native tissues is of critical importance for TE applications [1,2] Traditional techniques to prepare 3D scaffolds with low structural complexity include electrospinning, phase separation, particulate leaching, and gas foaming.1 In recent years, 3D scaffolds with more controlled microstructures have been constructed by 3D printing [3] Such techniques, however, cannot provide complex and fine features (e.g. patterns) on the nano- and micro-scales below 10 um to the 3D scaffolds [3,4]. The nano- and micro-scale architectures on the cell-attached surface enable to precisely control the cell activities including cell morphology, alignment, and differentiation, which is crucial for regenerating targeted functional tissues [5] Thus, in combination with other reported techniques, microfabrication techniques including photo/soft lithography and hot embossing are considered vital technologies for the preparation of 3D hierarchical scaffolds with combined macro/micro/nano structures [5a,6]. For example, Dvir et al. recently reported a 3D hierarchical TE

scaffold based on modular assembly of multiple layers with distinct structures and functions, in which each layer was prepared via both electrospinning and photolithography [5a].

Although 3D printing of polymeric materials has shown substantial progress for constructing complex 3D structures over conventional molding techniques, it still requires particular printers, specialized programs, and limited choice of materials [3]. Instead, directly converting 2D plastic materials into functional 3D structures without any special equipment is also of increasing interest, because it can take the advantages of planar films, in terms of mass production, storage, package, and transportation [7]. Moreover, compared to 3D structures, the planar films are easy to be nano- or micro-patterned via the mature microfabrication techniques prior to the 3D macro-shape constructing [5,6]. In order to transform the pristine 2D polymeric films into customized 3D hierarchical structures via simple heat-induced shape programming without any costly and complicated processing, the polymeric materials need to be processable like vitreous glass, not requiring precise temperature control unlike the conventional thermoplastics or polymer networks with dissociative cross-link exchanges [8]. Since Leibler et al. reported such a new class of polymer network materials (i.e. vitrimers) utilizing transesterification reactions in 2011 [9], a variety of associative cross-link exchange mechanisms have been studied extensively for achieving the glass-like

fluidity in permanent polymer networks [8,9]. There have been also several reports on the applications of the vitrimers including composites [10a], adhesives [10b], actuators [9], and nanogenerators [10c], but, to our knowledge, their TE scaffold application has not been explored yet.

Herein, we report the preparation of a vitrimer film (PAB-POSS vitrimer) for 3D hierarchical TE scaffolds, consisting of all biocompatible ingredients of rubbery poly(acrylonitrile-co-butadiene) (PAB) chains, inorganic polyhedral oligomeric silsesquioxane (POSS) cross-linkers, and Zn^{2+} catalysts (Fig. 4.1) [11]. By covalently cross-linking the dicarboxyl end groups of PAB with octaglycidyl functional groups of POSS, we have achieved tissue-like mechanical properties of Young's modulus ($E \approx 1.2$ MPa), extensibility ($\varepsilon_b \approx 80\%$), and elasticity (immediate and complete recovery of strain) as well as sufficient cell viability for the TE vitrimer. Microsized surface grooves as well as various macroscopic 3D structures of the PAB-POSS vitrimer are readily prepared via hot embossing patterning and thermal reconfiguration process, which utilize one of the most widely studied associative exchange mechanisms, Zn^{2+}-catalyzed transesterification [9,12]. In particular, the micro-patterned PAB-POSS vitrimer with a narrow groove width of ≈10 um greatly improves the elongation and alignment of the C2C12 mouse myoblasts, thus demonstrating its possible application in 3D hierarchical TE scaffolds.

4.2. Experimental

4.2.1. Materials

Dicarboxyl terminated poly(acrylonitrile-co-butadiene) (PAB) (average M_n ~3,800 g mol^{-1}, acrylonitrile 8-12 wt%) and zinc acetate was purchased from Sigma-Aldrich. Octaglycidyl functionalized polyhedral oligomeric silsesquioxane (POSS) was supplied by Hybrid Plastics. Chloroform ($CHCl_3$, 99.5 %) purchased from Dae Jung was used as received. Microgrooved nickel molds (dimension; 80, 40, and 10 um in a groove width with a constant depth of 5 um) were provided by SJ company in South Korea.

4.2.2. Preparation of the vitrimer film (PAB-POSS vitrimer)

A vitrimer film named as PAB-POSS vitrimer was prepared as follows. 5 g of PAB and zinc acetate (10 mol% to carboxyl group of PAB) were introduced into a 50 mL round-bottom flask with a magnetic stirring bar and heated at 130 ^oC under vacuum. The reaction proceeded for 2 h until no acetic acid gas was emitted and the zinc acetate was completely solubilized. 2.16 g of the compound (1.02 mmol acid + 0.11 mmol zinc acetate) was mixed with POSS (0.19 g, 1.13 mmol epoxy) using minimal amount of $CHCl_3$ at 50 ^oC for 1 h. The solution was poured into a

silicon mold (ca. 60 mm (L) × 60 mm (W) × 10 mm (T)) and stayed overnight until the solvent was completely evaporated. A 500 um thick vitrimer film could be obtained after a crosslinking reaction at 150 ^{o}C under vacuum for 20 h (gel fraction: 96.2 %).

4.2.3. Fabrication of the micro-patterned PAB-POSS vitrimer surfaces and 3D structures

Micro-patterned PAB-POSS vitrimers with groove widths of 80, 40, and 10 um, respectively, were prepared by pressing the corresponding microgrooved nickel molds onto the PAB-POSS vitrimer under vacuum at 180 ^{o}C for 6 h. 3D structures could be constructed by shaping the vitrimer film into the desired 3D geometry, and then placing them in the vacuum oven at 180 ^{o}C for 3 h. A tubular structure with micro-patterned outer surface was particularly prepared from the PAB-POSS vitrimer with 10 um groove width.

4.2.4. Cell culture

C2C12 muscle cells (ATCC® CRL-1772™) were cultured in Dulbecco's modified Eagle's medium (DMEM, Gibco, Grand Island, NY) supplemented with 10 % fetal bovine serum (FBS, Gibco BRL) and 1 % (v/v) penicillin/streptomycin (Gibco BRL).

4.2.5. Cytotoxicity test

Biocompatibility of the PAB-POSS vitrimer was determined by EZ-Cytox cell viability assay kit (Daeil Labservice, Korea) according to the manufacturer's protocol (n = 3 per group). 100 uL of the cell suspension was dispensed in a 24-well plate and pre-incubated for 24 h in a humidified incubator (at 37 ^{o}C, 5 % CO2). The circle-shaped sample (10 mm (D)) loaded inserts were immersed in each well and incubated for 24 and 48 h, respectively. A glass substrate of the same size was used as a positive control in this test. After replenishing with fresh medium, CCK-8 solution was added into each well of the 24 well plate, and the cells were incubated for 2 h. The cell viability was evaluated using a colorimetric test based on formazan dye generated by intracellular dehydrogenases, which is directly proportional to the number of the viable cells. In brief, 10 uL of EZ-Cytox solution was added to each well of the plate and incubated for 3 h in the incubator. The absorbance was read at 450 nm using a microplate reader (Bio-Tek, PowerWaveX340).

4.2.6. Cell alignment

C2C12 cells were seeded on the PAB-POSS vitrimer, and the micro-patterned PAB-POSS vitrimers at a density of 5.3×10^4 cells/cm^2, and cultured for 24 h. To

obtain field-emission scanning electron microscopy (FE-SEM) images, the cells on the substrates were fixed according to following protocol. Briefly, the cells rinsed with phosphate-buffered saline (PBS) were immersed in 3 % glutaraldehyde for 10 min at room temperature, followed by dehydration with ethanol. Ethanol was replaced by hexamethyldisilazane, and it was completely evaporated before analysis. The cell alignment was quantitatively analyzed using ImageJ software (National Institute of Health, Bethesda, MD, USA).

4.2.7. Instrumentation and characterization techniques

Infrared (IR) spectra were recorded on a Nicolet 6700 spectrophotometer (Thermo Scientific, USA) using attenuated total reflectance (ATR) equipment (FT-IR/ATR). The thermal transition behaviors of PAB-POSS vitrimer and PAB were examined by differential scanning calorimetry (DSC) using TA Instruments DSC-Q1000 under a nitrogen atmosphere. Dried samples with a typical mass of 3–7 mg were encapsulated in sealed aluminum pans. The samples were quenched to –80 °C for 5 min and maintained at this temperature for 5 min, then heated to 250 °C at a heating rate of 10 °C/min. The glass transition temperature (T_g) was taken as the point of inflection of the plot of the change in heat capacity with temperature in the DSC thermograms. The thermal stability of the vitimer film was investigated by thermogravimetric analysis (TGA) using TA Instruments

TGA Q-5000IR under a nitrogen atmosphere. 10 mg of the dried sample was heated to 700 ^{o}C at a heating rate of 10 ^{o}C/min. The mechanical properties of the PAB-POSS vitrimer were measured using a universal testing machine (UTM, Instron-5543, USA). Rectangular-shaped specimens (ca. 60 mm × 5 mm) were prepared using a cutting die, and the tensile properties of the films were measured at 25 °C under 40 % RH conditions with a gauge length and cross head speed of 20 mm and 10 mm/min, respectively. Cyclic tensile testing was performed on the same UTM using the same rectangular shaped film (gauge length = 20 mm) at a strain rate of 10 mm/min. Dynamic mechanical analysis (DMA) was performed on a TA Instruments DMA Q800 with attached cryo accessory using rectangular-shaped PAB-POSS vitrimer film (ca. 30 mm × 5 mm). DMA was conducted in the film tension mode with a 2.5 Hz frequency, 0.1 % strain, and 0.1 N axial force. The specimens were first cooled down from room temperature to –100 ^{o}C and then heated to 60 ^{o}C at a constant rate of 5 ^{o}C/min in a nitrogen atmosphere. Cross-linking density (ν_e) of the PAB-POSS vitrimer was calculated as

$$\nu_e = E' / 3RT \qquad (1)$$

where E', R, and T are the storage modulus, universal gas constant, and absolute temperature in the rubbery region (ca. 298.15 K), respectively. Stress relaxation experiments of the circle-shaped vitrimer film (ca. 8 mm (D), 1 mm (T)) was carried out at specified temperature (180–220 °C) using a rotational rheometer

(ARES-G2, TA Instruments, USA). The sample was allowed to equilibrate at each temperature for 10 min, then subjected to a constant strain of 10 % until it had reached to the relaxation time (τ*) which was defined as the time required for the stress relaxation modulus had relaxed to at least 37 % (1/e) of its initial value. A constant normal force of 2.0 N was applied throughout the measurement to ensure a good contact of the material with the geometries. τ* was determined via the stress relaxation analysis at varying temperatures from 180 to 220 °C. These points were then plotted vs. 1000/T and fit to the Arrhenius relationship as follows

$$\tau^*(t) = \tau_0 \, e^{E_a/RT} \qquad (2)$$

where τ_0 is the characteristic relaxation time at infinite t, E_a (kJ/mol) is the activation energy of the transesterification reaction, R is the universal gas constant and T is the absolute temperature at the experiment was performed. Freezing transition temperature (T_v) is defined as the point at which a vitrimer exhibits a viscosity of 10^{12} Pa s, also known as the liquid to solid transition viscosity (η). Using Maxwell's relation (Eq. 3) and E' (average storage modulus in the rubbery region) determined from DMA, τ* was determined to be ca. 1.3×10^6 s at T_v . The Arrhenius relationship from Eq. S2 was then extrapolated to $\tau^* = 1.3 \times 10^6$ to determine the T_v.

$$\eta = (1/3) \, E' \, \tau^* \qquad (3)$$

The surface morphologies of the microopatterned PAB-POSS vitrimer was analyzed using FE-SEM (Carl Zeiss SUPRA, Germany). All the samples were coated with platinum under vacuum prior to the measurement. The cross-section of the micropatterns was obtained using focused ion beam (FIB) milling combined with scanning electron microscopy (SEM, Carl Zeiss AURIGA, Germany) and the depth of the micropattern was measured at a tilted stage.

4.3. Results and Discussion

The PAB-POSS vitrimer was prepared via simple solution casting of the Zn^{2+}-coordinated dicarboxyl-PAB (average Mn = 3,800 g mol^{-1}) and octaglycidyl-POSS mixture in $CHCl_3$ onto a silicon mold, followed by drying at room temperature overnight and subsequent thermal treatment at 150 ^oC for 20 h under vacuum. The molar feed ratio of carboxyl end group of PAB to epoxy group of POSS ([carboxyl]:[epoxy]) was fixed at 1:1, wherein 10 mol% of the carboxyl groups were coordinated with Zn^{2+} ions. The Zn^{2+} ions work as a reaction catalyst during crosslinking of carboxyl and epoxy groups as well as participate in transesterification between hydroxyl and ester groups in the prepared vitrimer network [12]. The completion of crosslinking reactions between terminal carboxyl groups of PAB and glycidyl groups of POSS could be confirmed by Fourier transform infrared (FT-IR) spectroscopy, where the characteristic peak of epoxy at 850 cm^{-1} disappeared and the C=O stretching vibration peak of PAB shifted from 1712 cm^{-1} to 1738 cm^{-1} due to the formation of ester linkages between PAB and POSS after the thermal treatment (Fig. 4.2) [13]. The characteristic peak at 1640 cm^{-1}, corresponding to the C=C stretching vibration in PAB chains, is still observed in the PAB-POSS network, thus attesting the formation of cross-linked networks with ester linkages without any oxidation reaction during the preparation [13].

Thermogravimetric analysis (TGA) shows that the PAB-POSS vitrimer exhibits insignificant weight loss until above 300 ^{o}C, with 5 % weight loss occurring near 378 ^{o}C (Table 1 and Fig. 4.3a). Glass transition temperature (T_g) of the vitrimer film, determined by differential scanning calorimetry (DSC), is –66.2 ^{o}C, which is only slightly higher than that (–68.3 ^{o}C) of the wax-state PAB without the cross-linking (Table 1 and Fig. 4.3b). This indicates that thermal transition behavior of the PAB-POSS vitrimer is mainly determined by the large content of flexible PAB chains (92 wt%) rather than the smaller content of POSS. Also, the bulky POSS cross-linkers are known to exhibit excellent molecular level dispersion and cross-linking in polymer networks as well as provide additional free volume to the polymer chains [14], thus enabling dimensionally stable vitrimer film without significant decrease of the polymer chain mobility.

It is important for TE scaffolds to possess appropriate mechanical properties for supporting the structure of organs and preventing them from collapsing by the contractile forces generated by surrounding tissues [15a]. The average Young's modulus and strain at break of the PAB-POSS vitrimer measured using an universal testing machine (UTM) were found to be 1.2±0.1 MPa and 82±7 %, respectively, at room temperature (Table 1 and Fig. 4.4a). The modulus value of 1.2±0.1 MPa is consistent with those of a wide range of native biological tissues such as blood vessels (≈1 MPa) [15a]. Moreover, the vitrimer film can be strained

and recovered to a similar level to the femoral artery (63-76 %) (Fig. 4.4b) [15b], which requires the strong elasticity to withstand the stress of the blood flow or muscle tissues [15a]. Such combination of modulus, elongation, and elasticity makes the PAB-POSS vitrimer a suitable candidate for TE scaffold applications, especially for the muscle tissues.

While possessing highly integrated covalent network structure in terms of cross-linking density (ν_e = 249 mol m^{-3}) and gel fraction (f_g = 0.96) (Table 1 and Fig. 4.5) [12b], the PAB-POSS vitrimer shows stress relaxation behavior at elevated temperatures. The shear stress relaxation experiments were conducted on the vitrimer film in the linear viscoelastic regime until the sample had relaxed to 1/e (≈37 %) of the initial stress, where the relaxation time (τ^*) was determined (Fig. 4.6a) [9,12,16]. The temperatures varied between 180 and 220 ^oC, which are much lower than the thermal decomposition temperature of the vitrimer film (Fig. 4.3a). The Zn^{2+}-catalyzed transesterification reactions and resulting topology rearrangements allow the network to relax stresses more rapidly with increasing temperature [9,12]. The relaxation times (τ^*) of the vitrimer follow an Arrhenius relationship with the temperature (Fig. 4.6b and Eq. 2). The activation energy (E_a) for the Zn^{2+}-catalyzed transesterification in the PAB-POSS vitrimer, extracted from the Arrhenius plot, is ≈87 kJ mol^{-1}, which is consistent with those for Zn^{2+}-catalyzed transesterification of vitirmers in the literature [9,12]. The PAB-POSS

vitrimer was found to have topology freezing transition temperature (T_v) of 100 ^{o}C, at which the change from a viscoelastic solid to a viscoelastic liquid occurs due to the increasing rate of the transesterification reaction [12]. Therefore, post-patterning and reconfiguration of the pristine 2D vitrimer film can be achieved by deformation under thermal treatment at temperatures above 100 ^{o}C.

Firstly, microsized patterns with controlled groove widths on the PAB-POSS vitrimer film are prepared using a simple hot embossing technique (Fig. 4.7a). When the nickel master stamps having different microgroove widths of 80, 40, and 10 um with a constant depth of 5 um were hot pressed onto the vitrimer film at 180 ^{o}C for 6 h under vacuum, dimensions of the corresponding patterns were confirmed to be 79.4/78.5, 38.1/39.3, and 9.7/10.3 in the width/spacing (um), respectively, with a uniform microgroove depth of $\approx$3 um for all the samples (Fig. 4.7c-e and Fig. 4.8). Various macroscopic 3D structures are also prepared from the vitrimer film via thermal reconfiguration process (Fig. 4.7f). The 3D structures in the shape of helix, pinwheel, tube, and porous curved plates were constructed by shaping the 2D vitrimer film and fixing at 180 ^{o}C for 3 h under vacuum. This result indicates that the PAB-POSS vitrimer can be easily reconfigured into 3D structures without using any special facilities, but with several simple deformation methods such as twisting, bending, rolling, and cutting under thermal treatment. Furthermore, the possible fabrication of a 3D hierarchical TE scaffold, exhibiting

the macroscopic tubular blood vessel structure with microscale outer surface patterns, is demonstrated via sequential hot embossing patterning and thermal reconfiguration of the 2D PAB-POSS vitrimer (Fig. 4.7a and g). The 3D hierarchical macro/micro structure could be useful to build better biomimetic microenvironments for cells [1,5a]. The presence of microgroove patterns on the outer surface of the tubular structure is evidenced by the translucent appearance originating from the light reflection on the micro-patterned surface [17].

In order to utilize the post-patternable and reconfigurable PAB-POSS vitrimer for TE scaffolds, sufficient biocompatibility should be primarily met. The cell viability of the vitrimer scaffold, prepared from biocompatible PAB, POSS, and Zn^{2+} substances [11], was evaluated by performing cell counting kit-8 (CCK-8) assay for 24 h using C2C12 muscle cells (Fig. 4.9a). The cell viability of the vitrimer is almost same as that of the positive control (i.e. glass substrate). Moreover, an increase in the cell viability is observed after 48 h from both PAB-POSS vitrimer and glass substrate. This indicates that no toxic substance is released from the film, although some reactants, that are not fully covalently integrated, still remain in the network ($f_g = 0.96$).

In addition to the cell viability test, in vitro cell attachment behaviors on the PAB-POSS vitrimer with different microgroove widths were investigated. When the C2C12 cells are cultured on the vitrimer surfaces for 24 h, the elongation and

alignment of the cells exhibit strong dependency on the microgroove widths (Fig. 4.9b-e). The PAB-POSS vitrimers with flat and 80 um patterned surfaces induce negligible effect on the cell morphology or alignment. On the other hand, larger aspect ratio and better cell alignment are apparently shown on the micro-patterned PAB-POSS vitrimer with a narrower groove width. In particular, the cell elongation and alignment are significantly promoted on the vitrimer film with the narrowest groove width of 10 um, which is consistent with the results in the literature [18]. From the quantitative morphology analysis, the average aspect ratio of the cells on the 10 um patterned vitrimer surface was found to be 10.1, which is about 3.9 times larger than that on the non-patterned surface (Fig. 4.9f). In addition, the cells on the 10 um patterned surface are parallel-aligned with a relatively small standard deviation of 13.9 ^{o} to the orientation of the microgrooves, whereas those on the non-patterned surface are randomly spread with a wide angle distribution from 1.2 to 179.6 ^{o} (Fig. 4.10). It is well-known that the uni-directional cell elongation and alignment can encourage the differentiation of myoblasts into organized arrays of myotubes, which is highly required for the repair of damaged muscles [18a].

4.4. Conclusion

In summary, we have demonstrated that a 2D PAB-POSS vitrimer can readily transform into various 3D hierarchical TE scaffolds with controlled microsized grooves and macroscopic architectures via hot embossing and thermal reconfiguration process. The combination of rubbery PAB, multifunctional POSS crosslinker, and Zn^{2+} catalyst in the vitrimer film results in tissue-like mechanical properties and sufficient biocompatibility. Moreover, the post-micro-patterned PAB-POSS vitrimer with 10 um groove width exhibits significantly improved C2C12 cell elongation and alignment. We believe that the present work provides insight into the design and preparation of vitrimeric materials with advanced properties for 3D hierarchical TE applications. In particular, shape memory [8b] or liquid crystalline vitrimers [7a] hold great promise for shape transformation of cell-seeded 2D film into tailored 3D structures at around body temperature. 3D printing of rheologically engineered vitrimers [19] can also provide more complicated 3D hierarchical scaffolds; such studies are underway.

4.5 Reference

[1] K. Seunarine, N. Gadegaard, M. Tormen, D. O. Meredith, M. O. Riehle and C. D. W. Wilkinson, Nanomedicine, 2006, 1, 281–296.

[2] H. Fernandes, L. Moroni, C. V. Blitterswijka and J. D. Boer, J. Mater. Chem., 2009, 19, 5474–5484.

[3] L. G. Bracaglia, B. T. Smith, E. Watson, N. Arumugasaamy, A. G. Mikos and J. P. Fisher, Acta Biomater., 2017, 56, 3–13.

[4] D. J. Richards, Y. Tan, J. Jia, H. Yao and Y. Mei, Isr. J. Chem., 2013, 1, 805–814.

[5] (a) S. Fleischer, A. Shapira, R. Feiner and T. Dvir, PNAS, 2017, 114, 1898–1903; (b) Manuel Théry, J. Cell. Sci., 2010, 123, 4201–4213.

[6] (a) J. L. Charest, M. T. Eliason, A. J. Garcı´a and W. P. King, Biomaterials, 2006, 27, 2487–2494; (b) Y. Liu, X. Li, X. Qu, L. Zhu, J. He, Q. Zhao, W. Wu and D. Li, Biofabrication, 2012, 4, 015004.

[7] (a) Y. Yang, Z. Pei, Z. Li, Y. Wei and Y. Ji, J. Am. Chem. Soc., 2016, 138, 2118–2121; (b) Y. Yang, E. M. Terentjev, Y. Wei and Y. Ji, Nat Commun., 2018, 9, 1906.

[8] (a) W. Denissen, J. M. Winne and F. E. Du Prez, Chem. Sci., 2016, 7, 30–38; (b) W. Zou, J. Dong, Y. Luo, Q. Zhao and T. Xie, Adv. Mater., 2017, 29, 1606100.

[9] D. Montarnal, M. Capelot, F. Tournilhac and L. Leibler, Science, 2011, 334, 965–968.

[10] (a) Q. Chen , X. Yu , Z. Pei , Y. Yang , Y. Wei and Y. Ji, Chem. Sci., 2017, 8, 724–733; (b) M. Röttger, T. Domenech, R. Weegen, A. Breuillac, R. Nicolaÿ and L. Leibler, Science, 2017, 356, 62–65; (c) J. Deng, X. Kuang, R. Liu, W. Ding, A. C. Wang, Y.-C. Lai, K. Dong, Z. Wen, Y. Wang, L. Wang, H. J. Qi, T. Zhang and Z L. Wang, Adv. Mater., 2018, 30, 1705918.

[11] (a) S. Samantarai, A. Nag, N. Singh, D. Dash, A. Basak, G. B. Nando and N. C. Das, J. Elastomers Plast., 2018, 0095244318768644; (b) X. Pan, H. Gao, G. Fu, Y. Gao and W. Zhang, RSC Adv., 2016, 6, 23471–23478; (c) N. Ninan, A. Forget, V. P. Shastri, N. H. Voelcker and A. Blencowe, ACS Appl. Mater. Interfaces, 2016, 8, 28511–28521.

[12] (a) M. Capelot, M. M. Unterlass, F. Tournilhac and L. Leibler, ACS Macro Lett. 2012, 1, 789− 792

[13] R. Konnola, C. P. R. Nair and K. Joseph, J. Therm. Anal. Calorim., 2016, 123, 1479–1489.

[14] S.-J. Kwon, D.-G. Kim, J. Shim, J. H. Lee, J.-H. Baik and J.-C. Lee, Polymer, 2014, 55, 2799− 2808.

[15] (a) S. J. Lee, J. Liu, S. H. Oh, S. Soker, A. Atala and J. J.Yoo, Biomaterials, 2008, 29, 2891− 2898; (b) A. Hasan, A. Memic, N. Annabi, M. Hossain, A. Paul, M. R. Dokmeci, F. Dehghani and A. Khademhosseini, Acta Biomater., 2014, 10, 11–25.

[16] J. P. Brutman, P. A. Delgado and M. A. Hillmyer, ACS Macro Lett., 2014, 3, 607− 610.

[17] F. D. Arisoy, K. W. Kolewe, B. Homyak, I. S. Kurtz, J. D. Schiffman and J. J.Watkins, ACS Appl. Mater. Interfaces, 2018, 10, 20055–20063.

[18] (a) Y. Zhao, H. Zeng, J. Nam and S. Agarwal, Biotechnol. Bioeng., 2009, 102, 624–631; (b) L. Altomare, N. Gadegaard, L. Visai, M.C. Tanzi and S. Farè, Acta Biomater., 2010, 6, 1948–1957.

[19] Q. Shi, K. Yu, X. Kuang, X. Mu, C. K. Dunn, M. L. Dunn, T. Wang and H. J. Qi, Mater. Horiz., 2017, 4, 598–607.

Table 4.1. Characteristics of the PAB-POSS vitrimer.

	ν_e[a] (mol m^{-3})	f_g[b]	$T_{d,5\%}$[c]	T_g[d] (^oC)	E[e] (MPa)	σ_u[e] (MPa)	ε_b[e] (%)
PAB-POSS vitrimer	249	0.96	378	–66.2	1.2 ± 0.1	0.6 ± 0.1	82 ± 7

[a]Cross-linking density, calculated by $\nu_e = E' / 3RT$, where E', R, and T are the storage modulus, universal gas constant, and absolute temperature in the rubbery region (ca. 298.15 K, Fig. 4.5), respectively. [b]Gel fraction, obtained by $f_g = W_a / W_d$, where W_d and W_a are the weights of dried film before and after chloroform solvent extraction. [c]Decomposition temperature, defined as 5 wt% loss. [d]Glass transition temperature, determined by differential scanning calorimetry. eDetermined from tensile testing at room temperature (25 ^oC), where E, σ_u, and ε_b are Young's modulus, ultimate tensile stress, and strain at break, respectively.

.

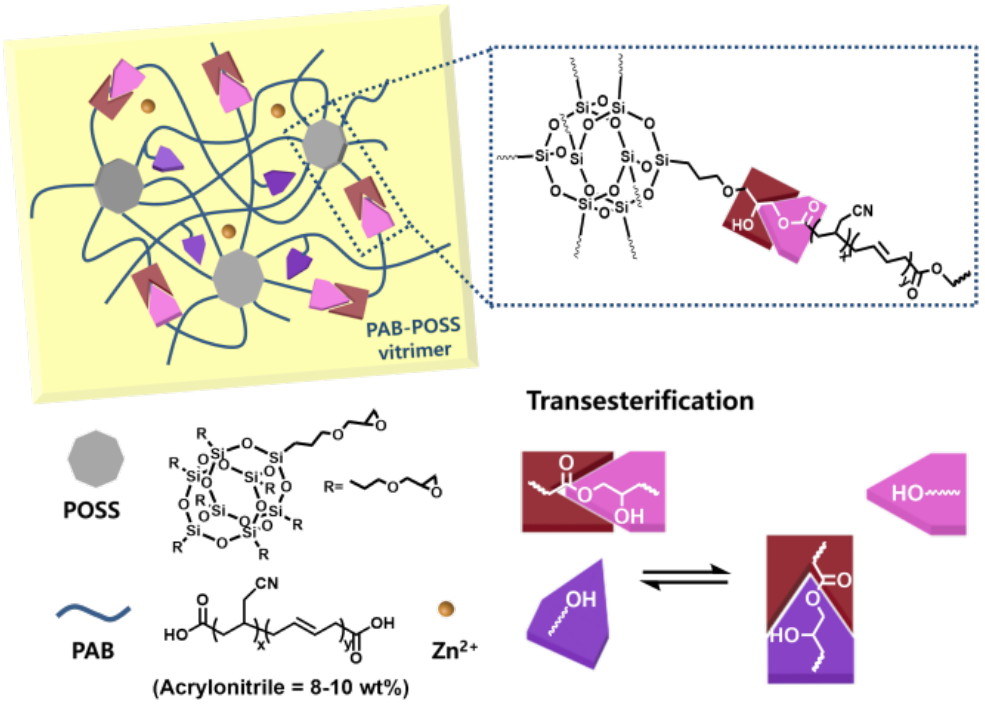

Figure 4.1. Schematic illustration of PAB-GPOSS vitrimer based on Zn^{2+}-catalyzed transesterification.

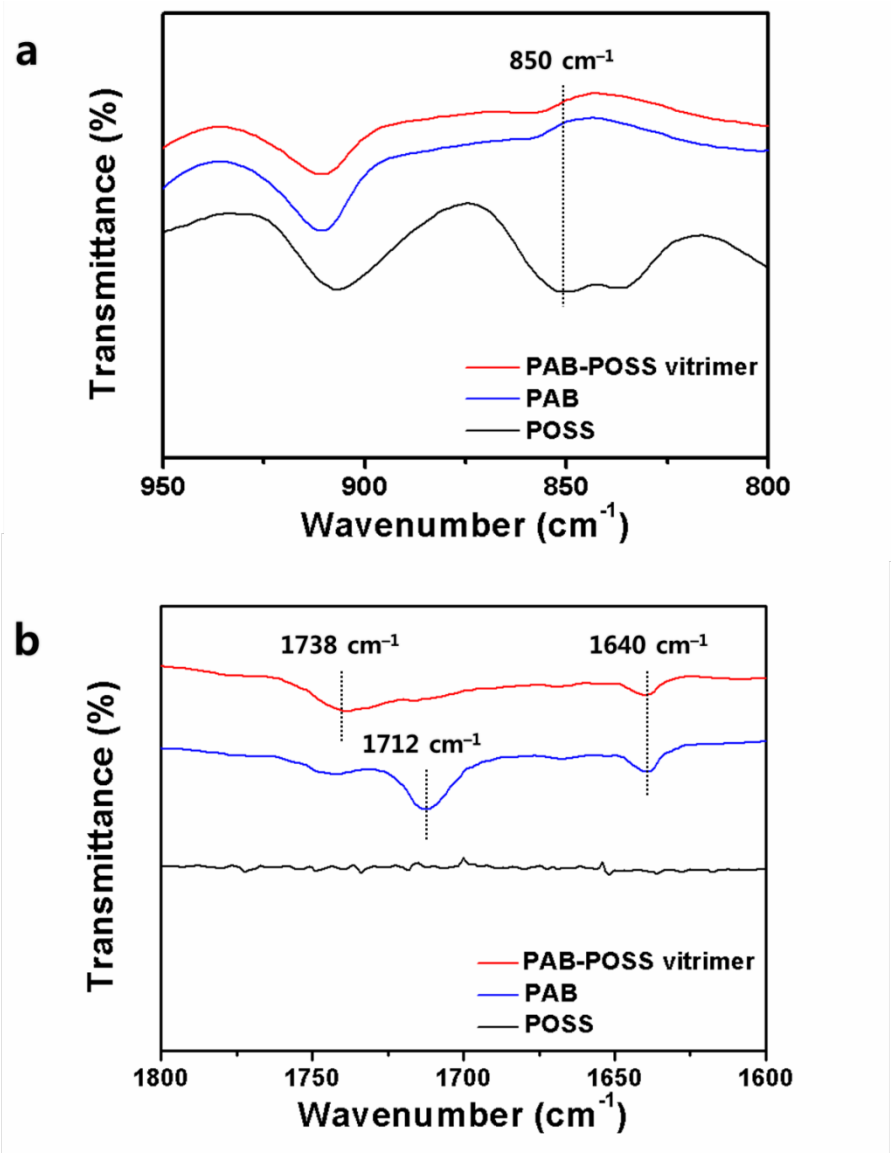

Figure 4.2. FT-IR spectra of the PAB-POSS vitrimer, PAB, and POSS in the wavenumber ranges of a) 950-800 cm^{-1} and b) 1800-1600 cm^{-1}, respectively.

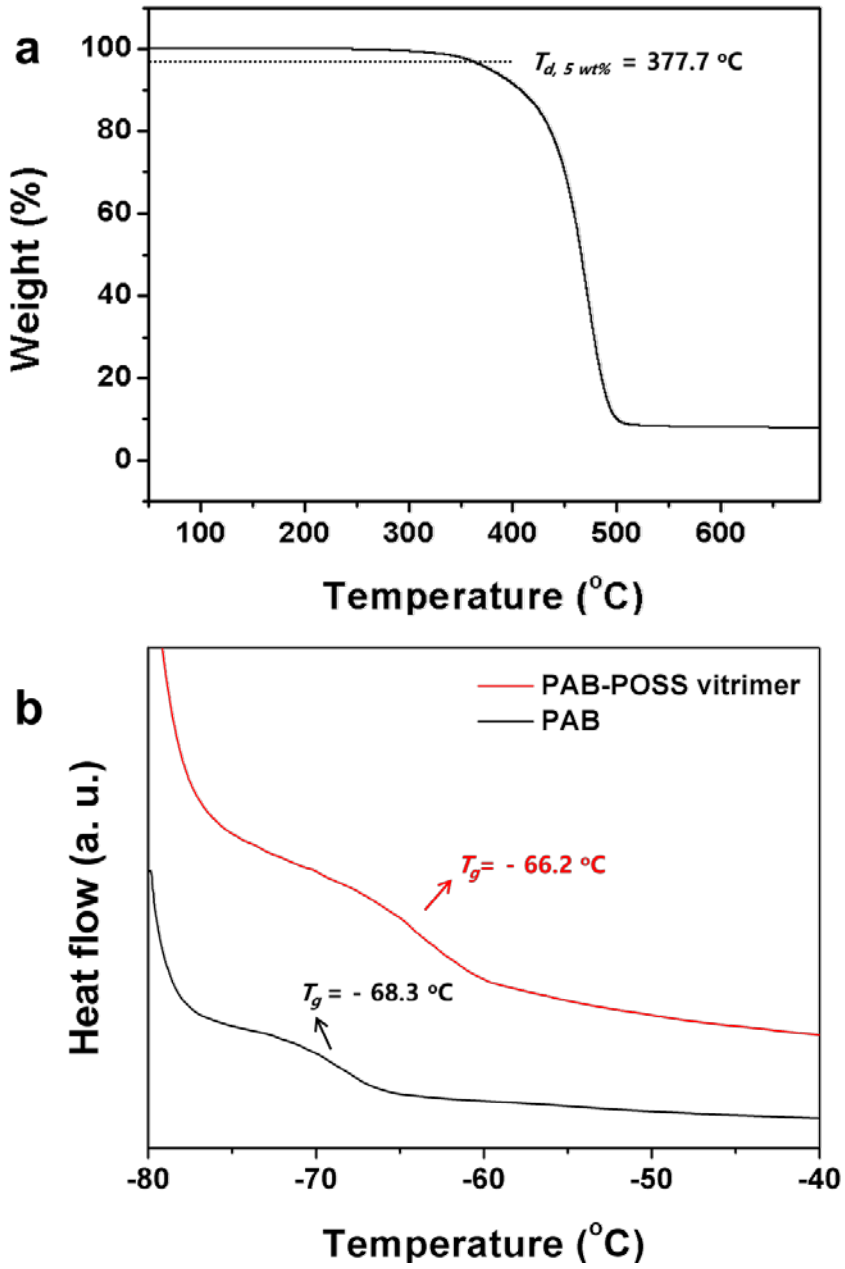

Figure 4.3. a) TGA thermogram of the PAB-POSS vitrimer and b) DSC traces of PAB and PAB-POSS vitrimer

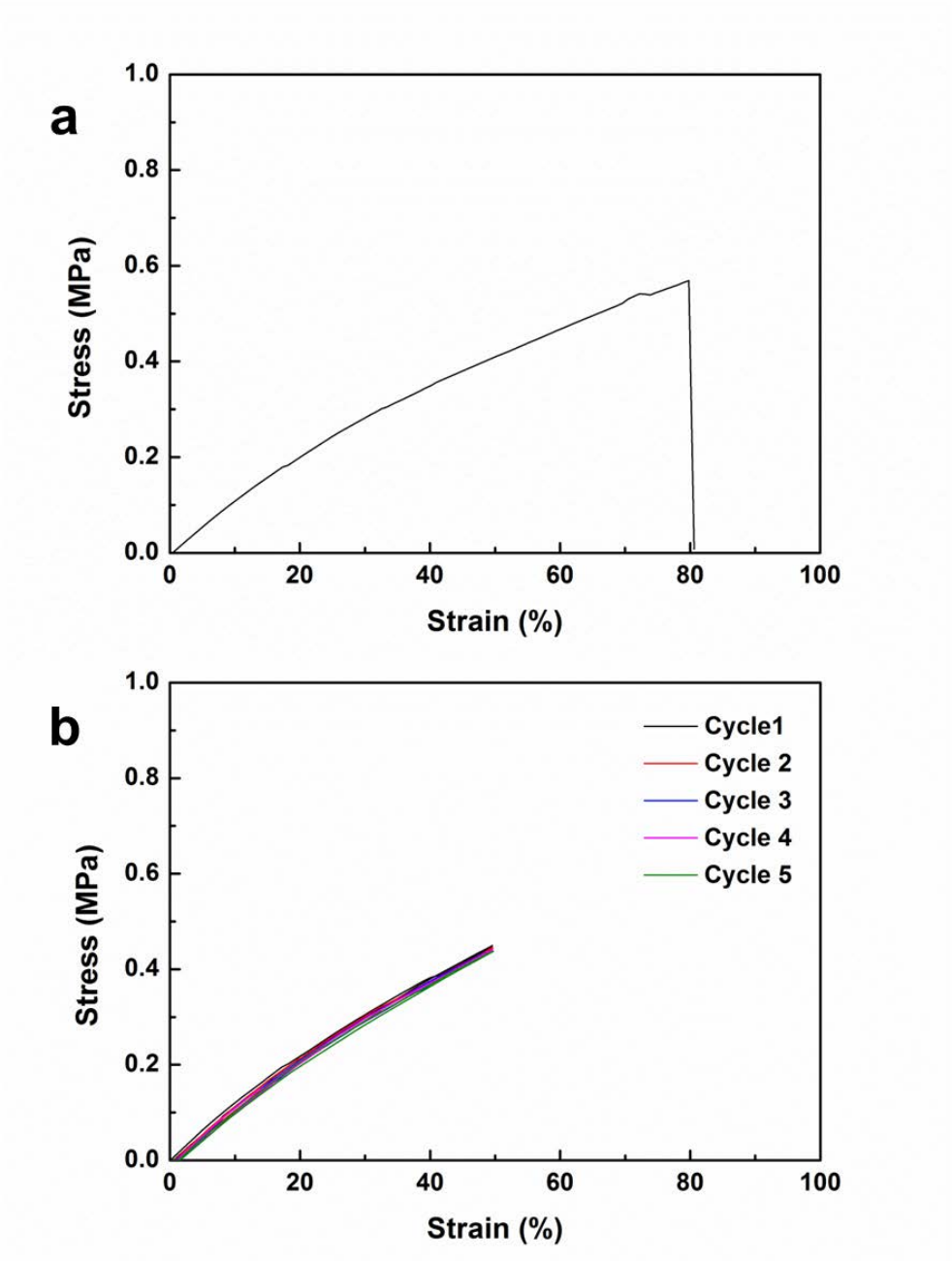

Figure 4.4. a) A representative stress-strain curve and b) cyclic stress-strain curves (strain limit = 50 %) of the PAB-POSS vitrimer.

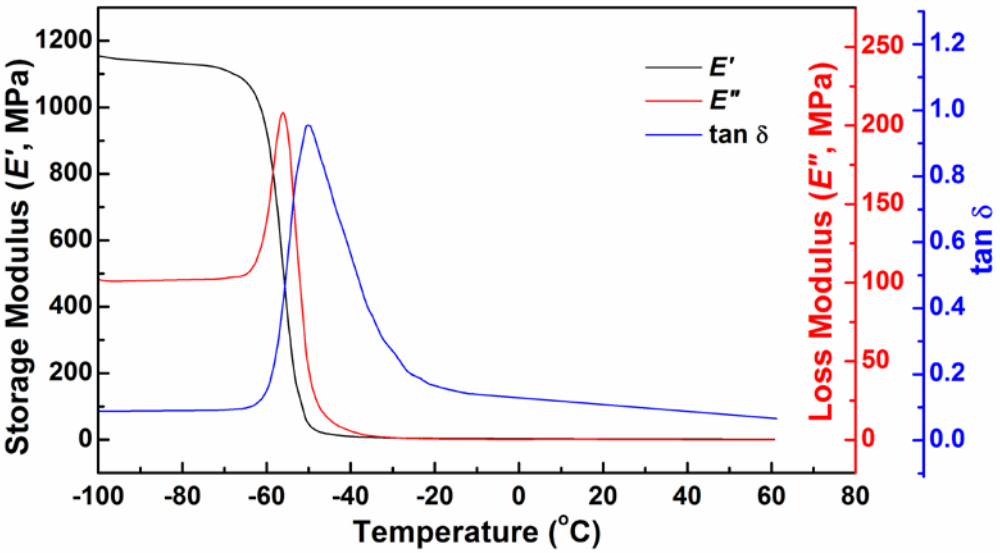

Figure 4.5. DMA curves of the PAB-POSS vitrimer.

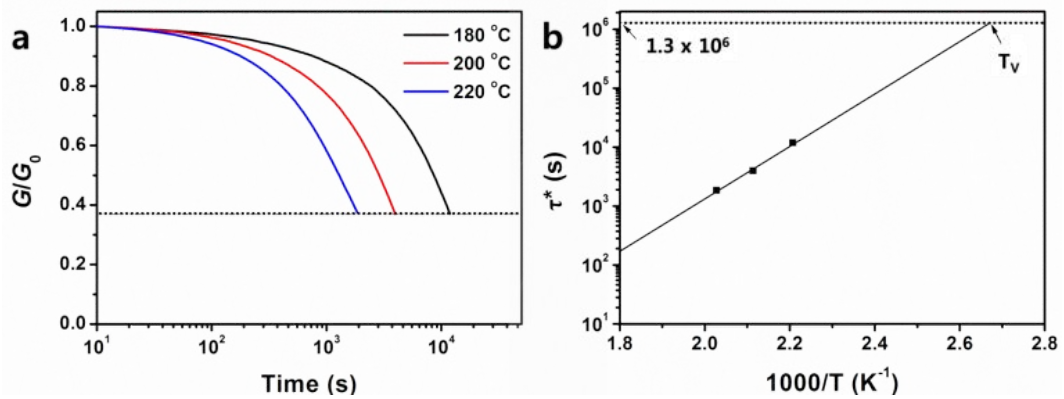

Figure 4.6 a) Normalized stress relaxation of the PAB-POSS vitrimer at different temperatures. The dashed line indicates $G/G_0 = e^{-1}$ (≈37 % of the initial stress). b) Arrhenius plot of the measured relaxation times for the PAB-POSS vitrimer.

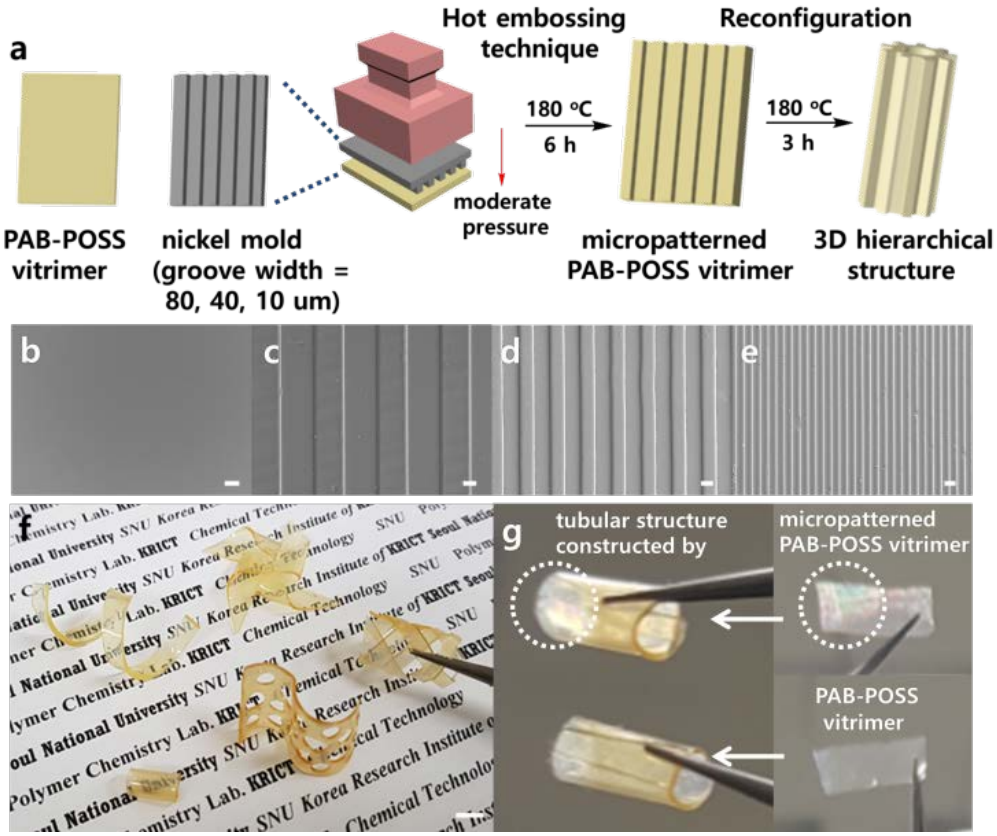

Figure 4.7. a) Schematic illustration for the fabrication of 3D hierarchical TE scaffolds from the PAB-POSS vitrimer via hot embossing techanique and thermal reconfiguration. Representative SEM images of the b) PAB-POSS vitrimer and micro-patterned PAB-POSS vitrimers with c) 80, d) 40, and e) 10 um groove width, respectively (scare bar= 20 um). f) Various 3D structures constructed by the PAB-POSS vitrimer (scare bar = 0.5 cm). g) A photograph of the tubular structure constructed by the 10 um patterned vitrimer film, which shows an unclear color at a certain light angle.

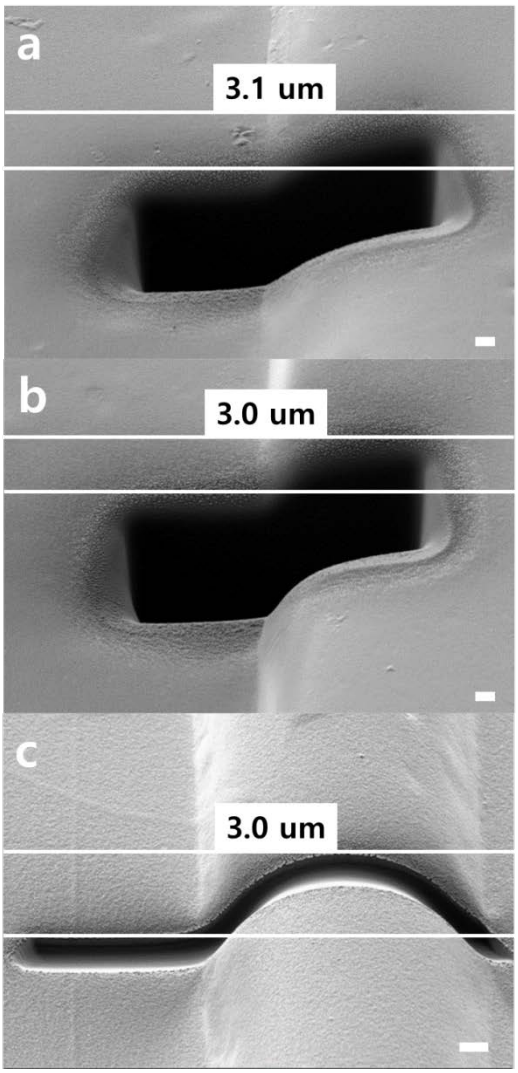

Figure 4.8. Representative SEM images of the cross-sections of PAB-POSS vitrimers with a) 80, b) 40, and c) 10 um groove widths, respectively. The cross-sections were obtained by FIB milling technique and the depth of each sample was measured at a tilted stage.

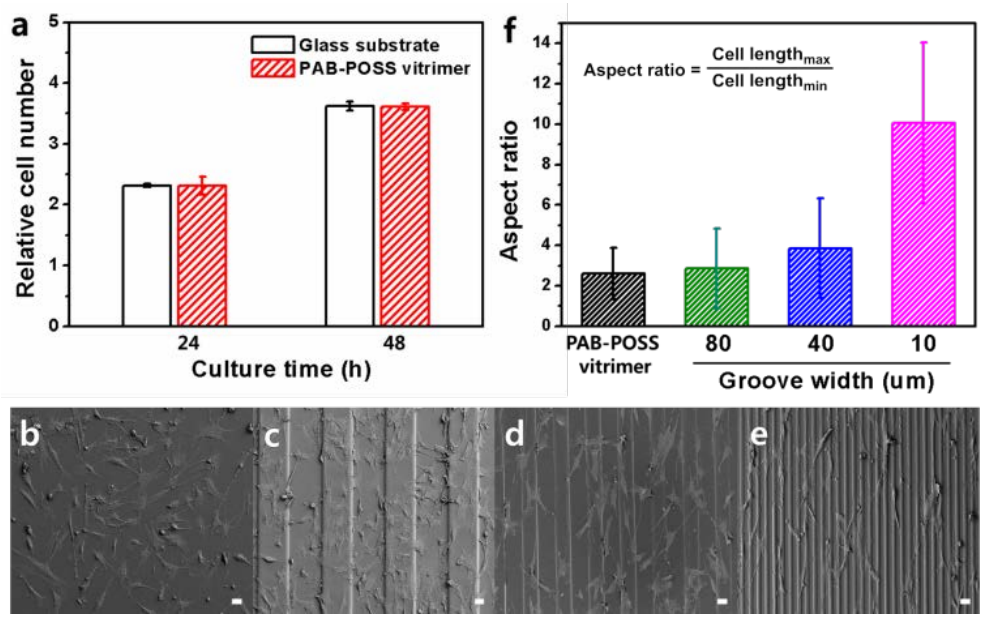

Figure 4.9. a) Cell viability of C2C12 cells cultured for 24 and 48 h on the glass substrate and the PAB-POSS vitrimer. Representative SEM images showing the morphology of C2C12 cells cultured for 24 h on the b) PAB-POSS vitrimers, and micro-patterned PAB-POSS vitrimer with c) 80, d) 40, and e) 10 groove width, respectively (scale bar = 20 um). f) Aspect ratios of the C2C12 cells cultured for 24 h on the PAB-POSS vitrimer and micro-patterned PAB-POSS vitrimers.

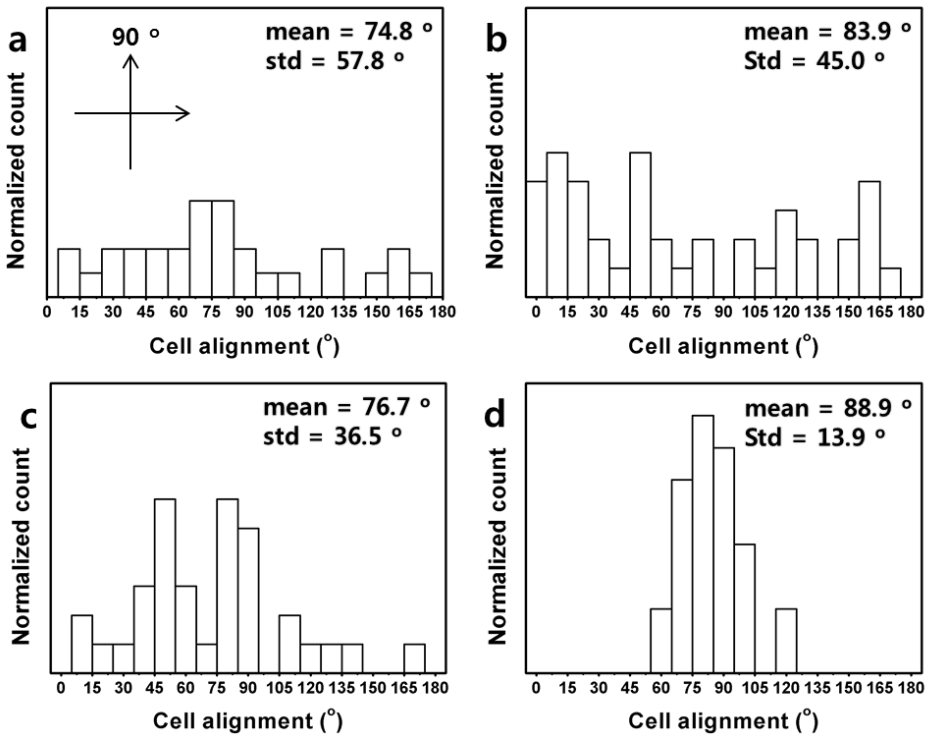

Figure 4.10. Quantitative analysis of the cell alignment on the a) pristine PAB-POSS vitrimer, and micro-patterned PAB-POSS vitrimers with b) 80, c) 40, and d) 10 um groove widths, respectively.

초 록

본 연구에서는 생체적합성 고분자를 합성하고 이를 2차원 전자기기 및 3차원 스캐폴드에 적용하는 연구에 대해 기술하였다. 첫째로, 생체적합성과 유기박막트랜지스터 (OTFT) 성질을 가지는 고분자 블렌드를 생체적합성 고분자, poly(2-(2-acetoxyacetyl)ethyl methacrylate) (PHEMAAA)와 전도성 고분자인 poly(3-hexyl thiophene) (P3HT)를 다른 비율 (i.e. P3HT/PHEMAAA = 75/25, 50/50, 25/75)로 섞어서 제작하였다. P3HT/PHEMAAA 블렌드 필름은 절연성을 가지는 PHEMAAA의 첨가에도 불구하고 순수한 P3HT와 비슷한 수준의 OTFT 성능을 유지함과 동시에, PHEMAAA 만큼의 우수한 생체적합성 또한 나타내었다. 특히, P3HT가 25 중량비가 블렌드 내에 포함되었을 때 최적의 OTFT 성능과 생체적합성을 보여주었다. 이러한 결과는 블렌드 비율에 따라 달라지는 고분자 배열, 형태 등의 필름 표면 성질과 밀접한 관련이 있는 것으로 확인되었다.

둘째로, 카다놀 기반의 고분자, poly(2-hydroxy-3-cardanylpropyl methacrylate) (PHCPM) 가 OTFT의 유전체로

사용되었다. PHCPM은 유전체에 적합한 우수한 표면 성질을 나타내며, 용액공정이 가능한 전도성고분자와도 안정된 계면을 이룰 수 있다. 따라서 유전체로 PHCPM을, 반도체로 PBTTT를 각각 적용한 플렉시블 OTFT는 구부러진 상태에서도 높은 모빌리티와 안정된 기기성능을 나타내었다.

마지막으로, 우수한 생체적합성과 기계적 강도를 가지는 고무기반의 비트리머 필름을 제작하여 3차원 스캐폴드에 적용하였다. 열에너지에 의해 활성화되는 트랜스에스터화 반응에 의하여 비트리머 필름이 재구성될 수 있으며, 이로 인해 마이크로패터닝이 가능할 뿐만 아니라 필름을 3차원구조로 제작가능함을 확인하였다. 마이크로패턴된 비트리머 필름 표면 위에서 근육세포인 C2C12의 행동을 관찰한 결과, 패턴 너비가 좁을수록 더 신장되고 패턴 방향으로 더 잘 배열됨을 확인할 수 있었다.

주요어: 생체적합성 고분자, 블렌딩, 조직공학, 가교구조, 비트리머, 유기박막트랜지스터, 3차원 스캐폴드, 마이크로패턴

학번: 2015-30209 성명: 김나경